Few-atomic-layered hexagonal boron nitride: CVD growth, characterization, and applications

Majharul Haque Khan[a], Hua Kun Liu[a], Xudong Sun[b], Yusuke Yamauchi[a], Yoshio Bando[c], Dmitri Golberg[c,d], Zhenguo Huang[*,a]

[a]Institute for Superconducting and Electronic Materials, University of Wollongong, Wollongong, NSW 2500, Australia. Email: zhenguo@uow.edu.au
[b]Key Laboratory for Anisotropy and Texture of Materials, Northeastern University, Shenyang, Liaoning 110819, China
[c]National Institute for Materials Science, Tsukuba, Ibaraki 3050044, Japan
[d]Queensland University of Technology, Brisbane, QLD 4000, Australia

Abstract

Two-dimensional (2D) materials have shown outstanding properties that make them the materials of choice for future semiconductor and flexible nanoelectronics. Hexagonal boron nitride nanosheet (BNNS) is one of the most studied 2D materials due to its extraordinary properties and potential applications. The synthesis of large, homogeneous, and few-layered BNNS, however, remains challenging. Among the various synthetic routes, chemical vapour deposition (CVD) is preferred on the grounds of its potential to yield large BNNS with controllable atomic layers and minimal contamination. We thus devote this review to the CVD growth of BNNS, and its characterization and applications. The recent progresses in the CVD growth of BNNS is firstly summarized from the aspects of precursors, substrates, growth mechanisms, and transfer techniques. This review then moves on to the characterization of few-atomic-layered h-BN sheets, covering a variety of microscopic and spectroscopic techniques that have proved useful for assessing the quality of BNNS. The applications of the BNNS are also summarized. This review is expected to instigate new methods and improvements in relation to the CVD growth of BNNS, which has enabled exceptional performance as a key component of nanoscale electronics.

Keywords: Hexagonal boron nitride, CVD, 2D materials, Nanosheets

1. Introduction

Dimensionality is an important feature for any material. One of the early zero-dimensional (0D) materials was fullerene, which was synthesized in 1985 [1]. Later on, in 1991, the one-dimensional (1D) carbon nanotube was synthesized, which is one of the most studied materials over the last two decades [2]. Following the invention of 0D fullerene and 1D carbon nanotube, the only missing part in the reduced dimensional family was two-dimensional (2D) materials. Although there have been reports on the synthesis of 2D materials since the early 1960s [3–5], the field did not gain enough attention until the discovery of graphene in 2004 [6].

Over the last decade, there has been an exponential increase in 2D materials research. Graphene occupies the largest portion of research output in the world of 2D materials. This is attributed to the exceptional properties of graphene, which primarily include ballistic charge carrier mobility (> 200,000 $cm^2V^{-1}s^{-1}$), excellent mechanical strength, remarkable thermal conductivity, etc. [7]. The other 2D layered materials include hexagonal boron nitride (*h*-BN), transition metal dichalcogenides (TMD, including MoS_2, WS_2, $MoSe_2$, WSe_2, etc.), transition metal oxides [8,9], and the buckled atomic crystals denoted as 'Xenes' (silicene [10], phosphorene [11,12], and germanene [13]). In addition, there may be hundreds of other 2D materials yet to be discovered [14].

2D materials have shown outstanding properties that make them the materials of choice for future semiconducting and flexible nanoelectronics [15]. The necessity of ultra-thinness, flexibility, and energy efficiency in these applications has put the use of 2D materials at the forefront. Nevertheless, 2D materials are unable to support themselves due to their atomic scale thickness, while the use of conventional bulk substrates as supports drastically reduces their performance. For example, the simple act of putting graphene on top of an SiO_2/Si substrate causes scattering of the electrons due to the dangling bonds and roughness of the SiO_2 surface, which, consequently, reduces its carrier mobility considerably [16]. Using *h*-BN as a support in preference to SiO_2/Si has improved the transport properties of graphene by at least an order of magnitude [16,17]. This is because *h*-BN is sp^2 bonded, atomically flat, devoid of dangling bonds, and an insulator. A significant number of subsequent publications reported the use of *h*-BN as a dielectric layer in graphene-based transistors [18–22]. Recent findings indicate that to realize future graphene-based nanoelectronics applications, simultaneous development of all the related 2D materials is essential.

In this review, we have summarized the structural information on few-atomic-layered *h*-BN nanosheet (BNNS), its synthesis, characterization, and applications. The chemical vapour deposition (CVD) method has proven to be the most effective technique for large-scale synthesis of high-quality BNNS. Therefore, the emphasis has been placed on the progress on CVD grown BNNS. The major challenges in the CVD growth of BNNS are as follows: obtaining impurity- and defect-free nanosheet, maintaining large-scale homogeneity and single crystallinity, and controlling the thickness. Also, methods for defect-, impurity-, and crack-free transfer of the as-grown BNNS to various substrates need to be developed for successful integration of BNNS into heterostructures with other 2D materials. Techniques for characterizing few-layer BNNS are also included in this review, since they are different from those applicable to bulk BN in many aspects.

2. Structural information on bulk boron nitride

Boron nitride atomic orbitals can be either sp^2 or sp^3 hybridized, thus producing several crystalline forms. BN forms hexagonal (*h*) and rhombohedral (*r*) lattices via sp^2 hybridized bonding and forms cubic (*c*) or wurtzite (*w*) lattices via the sp^3 hybridization configuration. Of these, the *h*-BN and *c*-BN forms are stable and are readily available [23]. Two less ordered sp^2 configured polymorphs, amorphous (*a*)-BN and turbostratic (*t*) BN, can form during the synthesis of *h*-BN and *r*-BN. *a*-BN appears due to structural disorder introduced at the atomic level. Therefore, *a*-BN can be considered to be disordered *h*-BN and is unstable in air, reacting with water vapour to form boric acid, boric oxides, and hydroxides [24]. *t*-BN, on the other hand, forms due to a fault in the *c* axis orientation of the *h*-BN layers (less or no ordering between the basal planes in subsequent layers) [25]. Most of the time, the interlayer spacing in *t*-BN is larger than those of *h*-BN and *r*-BN, and thus, only in-plane ordering of atoms is possible in *t*-BN. This type of BN has also been reported to be unstable after long-term exposure to air, forming ammonium borate compounds ($NH_4B_5O_8.4H_2O$) [26].

3. Nanostructured boron nitride

Similar to the carbon allotropes of graphene, carbon nanotube, and fullerene, *h*-BN can form BNNS [8], BN nanotube [27], and BN fullerene [28]. In addition, various morphologies, such as nanoribbons [29,30], nanoplates [25,31], nanowires [32], nanofibers [33], nanoropes [34], nanocups [35], nanofunnels [36], nanomikes [36], microbelts [37], and foams [38], have been reported.

BNNS is few-atomic-layered BN, in which in-plane hexagonal arrangements of B and N atoms occur. Due to the remarkable structural similarity to graphene (bond length and interlayer distance), single layer hexagonal boron nitride is also called 'white graphene'. The difference in electronegativity between the B (2.04) and N (3.04) atoms results in the B-N bond being slightly ionic in nature.

The 2D *h*-BN can be either zigzag or armchair edge terminated (Figure 1a, b) [39]. BNNS generally grows as triangular sheets on transition metal substrates, which result in a chemically unbalanced state along the sheet edges, i.e., either B terminated or N terminated edges. For the BNNS grown on Cu substrate, the N terminated zigzag edge is found to be more favourable than the B terminated one (Figure 1c) [40], thus producing equilateral triangles during the growth. In contrast to the more favourable zigzag edge termination in BNNS, the armchair edge termination is found to be energetically stable in *h*-BN nanoribbon (Figure 1d) [41,42].

Depending on the B to N ratio in the precursor, the substrate, and the lateral size, the equilateral triangle can be transformed to truncated hexagonal shapes, where both N and B terminated edges can be energetically stable (Figure 1e, f, h) [43,44]. For the BNNS on Ni substrate, the B terminated edge structure can be more stable than the N terminated edge (Figure 1g) [43]. Experimental evidence is yet to be reported to confirm the latter case.
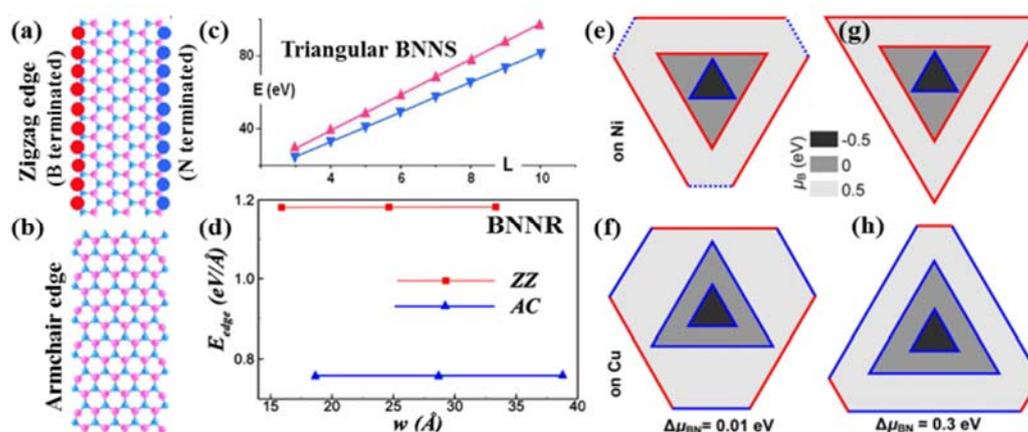
Figure 1: Schematic representation of (a) zigzag and (b) armchair edge terminated *h*-BN. (c) Calculated total energy in the triangular BNNS, as a function of the sheet size, L. The N terminated zigzag edge is more favourable than the B terminated zigzag edge in the BNNS as the nanosheet size increases. Adapted with permission from ref. 39. Copyright 2011 American Chemical Society. (d) In *h*-BN nanoribbon (BNNR), the armchair edge is simulated

to be much more energetically stable than the zigzag edge. 'ZZ' and 'AC' refer to the zigzag and armchair edges, respectively. Adapted with permission from ref. 41. Copyright 2011 American Chemical Society. (e-h) Simulated shape and edge orientations of h-BN on Ni and Cu substrates in respect to the B potential (μ_B) and the degree of nonequilibrium conditions ($\Delta\mu_{BN}$). Formation of truncated triangles (e, f, and h), B and N terminated edges (e, f, and h) and only B terminated edges (g, only on Ni substrate) is thermodynamically possible. Adapted with permission from ref. 43. Copyright 2016 American Chemical Society.

3.1. Stacking in BNNS

Although h-BN is isostructural to graphite, there is a stacking order difference between these two materials. While graphite is a Bernal stacked (AB) structure, h-BN in a bulk scale is generally considered to be AA´ stacked (B atom on top of N atom and vice versa). BNNS has been predicted to adopt other stacking orders, however [45]. Bernal stacked AB or AC, similar to graphite, is reported to be energetically favourable, in addition to the AA´ stacking [46,47]. Both of these stacking orders have been detected using dark field – transmission electron microscopy (DF-TEM)[45] in CVD grown h-BNNS (Figure 2a). The AB stacking order in BNNS has also been found in chemically exfoliated BNNS through high angle annular dark field – scanning TEM (HAADF-STEM) Z-contrast imaging. The AB stacking order has been attributed to the presence of impurities in the chemically exfoliated layers, which might have assisted in transforming the AA´ stacking to AB stacking (Figure 2b) [48]. In a recent publication, we have reported the observation of AB, ABA, AC´, and AC´B stacked BNNS through HAADF-STEM analysis for CVD grown multilayered BNNS on solid Cu substrates at 1000 °C (Figure 2c) [49]. Among these stacking orders, AC´ stacking is generally considered the least energetically favourable of all the stacking configurations in h-BN. It has been suggested that under the high-temperature CVD growth conditions, the electrostatic forces that dictate the optimal stacking mode in h-BN [50] are disturbed by the high kinetic energies of the atoms, and the film may adopt various stacking orders [47]. More work needs to be carried out to understand the exact origin of various h-BN stacking orders. Growing BNNS on other substrates such as Ni, Fe, and Pt, and comparing the stacking order with that grown on Cu may help to explain the impact of substrates on stacking orders. HAADF-STEM analysis, combined with scanning electron microscopy (SEM) and electron backscattered diffraction (EBSD) results may help to clarify the impact of substrate grain orientation on the stacking order. Stacking order dependent property variations of the BNNS have been documented in the literature [45]. For example, optical and topological properties change when the stacking order changes from AA´ to AB in

h-BN [45]. To use BNNS as a substrate for graphene-based nano- and opto-electronics applications, the impact of different stacking orders remains to be studied.

Various stacking orders in other CVD grown 2D materials have also been observed [51–53]. For example, in GaSe crystal, AB stacking (ε polytype) is considered the most energetically favourable. Experimentally, the less energetically favourable AA´ stacking (β polytype) has also been found [51]. Both AA´ and AB stacking orders have been reported for 2D MoS_2 also, where AA´ stacking is considered the most common [52,53].
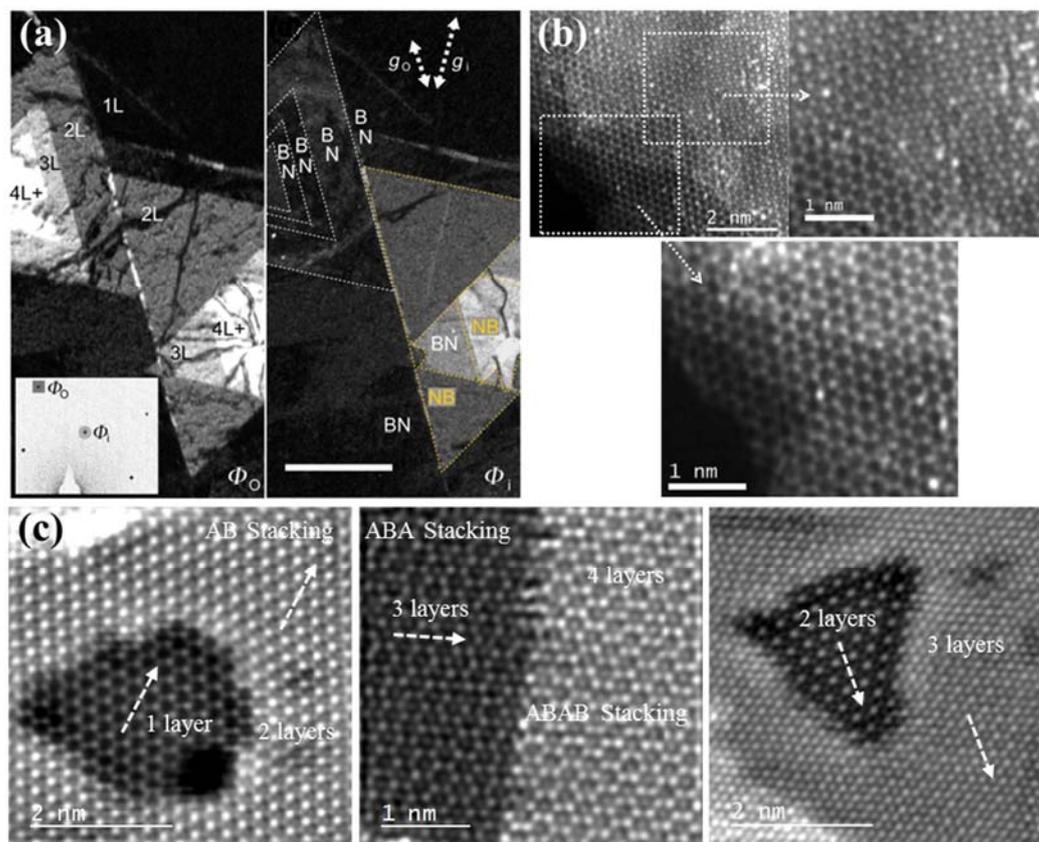
Figure 2: Observations of various stacking orders in BNNS. (a) DF-TEM images, obtained by selecting the φ_0 (left image) and φ_i (right image) diffraction spots, respectively. The left and right multilayered triangles in each image are AB and AA´ stacked, respectively. Adapted with permission from ref. 45. Copyright 2013 American Chemical Society. (b) HAADF-STEM observation of AB and AA´ stacking orders in the two regions of chemically exfoliated BNNS. Adapted from ref. 48 with permission from The Royal Society of Chemistry. (c)

HAADF-STEM observations of AB, ABA, ABAB, AC′, and AC′B stacking in CVD grown BNNS. Adapted from ref. 49 with permission from The Royal Society of Chemistry.

3.2. Defects in BNNS

Defects in a 2D system can have more far-reaching effects than in its bulk counterpart. This is because nearly all the atoms are in the surface, especially in the case of monolayers, and perturbation of the surface atomic arrangements due to defects can change the properties dramatically. For example, the presence of Stone-Wales type line defects (pentagon-heptagon pairs, 5/7) in BNNS can lower the band gap significantly [54]. Also, defects have been assigned as the possible cause for the very low elastic modulus [55] and bending modulus [56] in CVD grown BNNS.

In 2D materials, where mono- to few-layer cases are mostly considered, the term 'grain boundary' which is a three-dimensional construct, is often replaced with 'domain boundary'. A polycrystalline 2D material is thus made up of various domains connected along the domain boundaries. The Stone-Wales type defect, which is very common for graphene, was predicted to be energetically less favourable than the square-octagonal pair (4/8) line defects in BNNS, due to the unfavourable homo-elemental bonding formations (B-B or N-N bonds) [57,58]. Depending on the tilt angle of the domain boundaries, however, both 4/8 (unpolar) and 5/7 (polar, B-rich or N-rich) defects are found to be energetically viable in BNNS from density functional theory (DFT) calculations [59]. In recent publications, both 4/8 and 5/7 type domain boundaries were experimentally observed by scanning tunnelling microscopy (STM) [54] and high-resolution TEM [55,60] analysis (Figure 3). Possible atomic configurations in the 4/8 and 5/7 type domain boundaries have been proposed (Figure 3c) [54]. Among these configurations, 4/8 type polar domain boundaries (Figure 3d, Type II) have been discovered [60], while the other configurations are yet to be confirmed experimentally.

Other common defects in 2D material are the point defects. In the case of BNNS, due to the presence of heteroatoms, the point defects can be either B/N vacancies or B/N-rich point defects [61]. Boron monovacancies are often induced by the high energy electron beam during the high resolution TEM (HRTEM) imaging [62–65]. By focusing the high energy electron beam in the boron monovacancy regions for a few minutes, further N and B atoms can be knocked out of that layer, leaving a triangular hole [62–65].
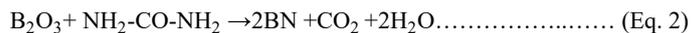
7
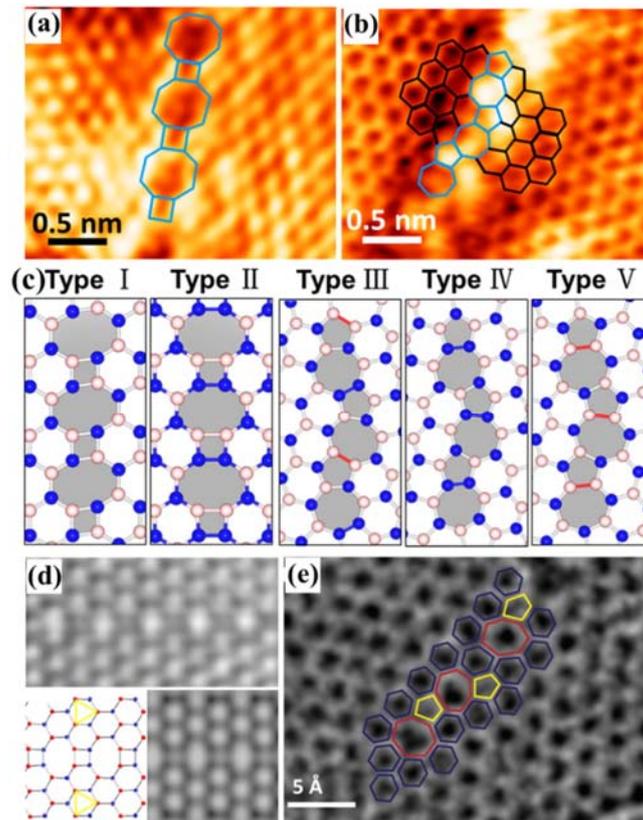
Figure 3: (a) 4/8 and (b) 5/7 type defects in the domain boundaries of BNNS, as confirmed by STM analysis. (c) Proposed atomic configurations for 4/8 (types I and II) and for 5/7 (types III-V) Adapted with permission from ref. 54. Copyright 2015 American Chemical Society. (d-e) HRTEM analysis of domain boundaries in BNNS, consisting of (d) polar 4/8 type (Adapted with permission from ref. 60. Copyright 2014 American Chemical Society) and (e) 5/7 type defects (Adapted with permission from ref. 55. Copyright 2013 American Chemical Society).
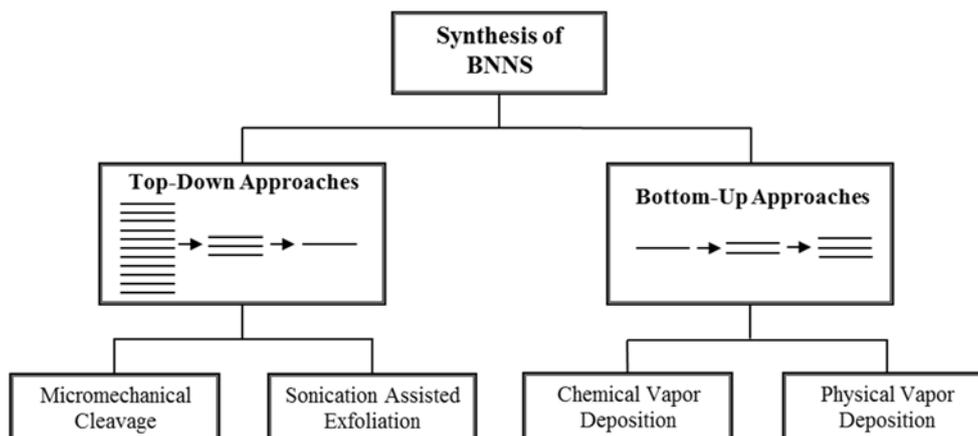
4. Synthesis of BNNS

Boron nitride was first synthesized in 1842 by the reaction between boric oxide and potassium cyanide [66]. Nowadays, the most popular commercial method of synthesizing h-BN powders is by heating boric acid/boric oxide and an ammonia/melamine/urea mixture at 900 °C, followed by annealing at 1500 °C in N_2 to increase the crystallinity of the powders [67,68].

$$B(OH)_3/B_2O_3 + NH_3 \rightarrow BN + H_2O\ldots\ldots\ldots\ldots\ldots\ldots\ldots\ldots\ldots\text{(Eq. 1)}$$

$$B_2O_3 + NH_2\text{-}CO\text{-}NH_2 \rightarrow 2BN + CO_2 + 2H_2O\ldots\ldots\ldots\ldots\ldots\text{(Eq. 2)}$$

Interest in the synthesis of 2D *h*-BN started immediately after the discovery of graphene in 2004. Broadly speaking, there are two methods to form BNNS: top-down, where bulk *h*-BN is exfoliated and/or thinned, and bottom-up, where B and N atoms form few-layered *h*-BN (Figure 4).

Figure 4: Common methods for the synthesis of BNNS.

4.1. Top-down approaches

This method is to exert certain forces (shearing force for example) to overcome the van der Waals forces that hold BN layers together. This method is useful for large-scale production of BNNS, but it generally produces BNNS with a large distribution of layer numbers, various lateral sizes, and contamination.

4.1.1. Micromechanical cleavage

Scotch tape has been used to peel off layered materials (graphite, BN, MoS_2, $NbSe_2$, and $Bi_2Sr_2CaCu_2O_x$) down to mono- and few-layers [8]. This technique can lead to BNNS with large lateral size and relatively free of contamination (aside from the tape adhesive which can be removed by a thermal anneal). BNNS obtained in this way can be easily stacked on top of another 2D material. For example, flexible field effect transistors (FETs) prepared by stacking exfoliated BNNS and graphene, have shown exceptional room temperature carrier mobility [16,69,70] and flexibility [70].

4.1.2. Sonication assisted exfoliation

Sonication was found to be an effective route to weaken the van der Waals forces between the layers in highly oriented layered materials. An extensive study of sonication-assisted exfoliation was conducted by Coleman et al [9]. The efficacy towards exfoliation and retention in a particular solvent was found to be dependent on the solvent's surface tension. During the sonication, ions and compounds were found to be intercalated between the BNNS layers [71–74]. Sonication in the presence of solvents has also proved to be very effective in functionalizing BNNS. For example, functionalization and exfoliation have been achieved using octadecylamine (ODA) [75]. Functionalization was achieved due to the strong Lewis acid-base interactions between electron-deficient boron and electron-rich amine molecules.

4.2. Bottom-up approaches

4.2.1. Chemical vapor deposition

The synthesis of *h*-BN thin film by the CVD process can be dated back to the early 1970s [76], when the CVD process became popular for the preparation of thin films [77]. Several reports were published afterwards, where micron-thick *h*-BN films were prepared on various substrates by the CVD process [78–82]. Single atomic layer BN was first grown by CVD in an ultra-high vacuum (UHV) system in 1995 [4,5]. Probably due to the complexity of the UHV system, the synthesis of atomic-layer-thin BNNS did not gain significant attention until recently. Significant progress has been made in growing high quality BNNS via low pressure (LP) - and atmospheric pressure (AP)-CVD.

CVD has been deemed to be the most effective method to grow large BNNS sheets with controllable atomic thickness. This is particularly important for nanoscale electronics where BNNS is used as the substrate. Several key CVD parameters exert dramatic effects on the quality of the BNNS. In this review, the impact of various precursors, substrates, and the treatments of substrates are discussed, since these are important and can be adjusted or tuned, regardless of the physical features of the CVD system. We have also summarized the growth mechanism of BNNS on transition metal substrates and the transfer techniques used to attach BNNS onto various substrates.

4.2.2. Precursor for BNNS synthesis

The precursors used to grow BNNS are listed in Table 1. The main precursor for the CVD synthesis is borazine,

which is isostructural to benzene. Intermolecular dehydrogenation at elevated temperatures fuses the six membered rings together into extended h-BN. Borazine, however, reacts with the moisture in air and can polymerize into solid polyborazylene [83]. Therefore, it needs to be stored under cold conditions in an inert atmosphere, which limits its use as a direct precursor for synthesis. One of the borazine derivatives, β-trichloroborazine, has been used [40,84]. The major drawback of this precursor is the release of HCl gas when it is exposed to humid air, which is corrosive to the CVD fittings and equipment.

Ammonia borane has been widely used as the CVD precursor to grow BNNS [44,56,85–88]. This compound is relatively air-stable, relatively non-toxic, and easy to handle. Ammonia borane decomposes to borazine, along with hydrogen, polyaminoborane, polyiminoborane, diborane, and ammonia, at around 110˚C [89,90]. The solid decomposition products can be prevented from reaching the reaction zone by decomposing ammonia borane in a flask fitted with a valve and a filter, all of which sit outside the furnace [20,56,86,88,91,92].

In addition to the above single-compound precursor containing both B and N in a 1:1 ratio, multiple-compound precursors have also been used for the synthesis of BNNS. For example, BF_3, N_2, and H_2 have been used to synthesize vertically aligned BNNS by the microwave plasma (MP)-CVD process [93–95]. The vertical alignment of the nanosheet on silicon wafers is probably induced by the electric field generated in the plasma sheath. The nanosheet thickness was controlled by varying the gas ratios. With a similar mechanism, gaseous BCl_3, NH_3, N_2, and H_2 were used to synthesize BNNS [96]. Diborane and ammonia as two gas-source precursors have also been employed [76,78–82]. These precursors were recently used in an LP-CVD system to synthesize few-layer BNNS on Ni and Cu foils [97]. BNNS grown on Cu foil was found to be turbostratic, while crystalline BNNS with controlled thickness was found on Ni foil. Decaborane and ammonia have also been used to synthesize few-layer BNNS [98]. Decaborane was used to take advantage of its stability in air and easy sublimation between room temperature and 90°C, with no other decomposition products being formed. In a three-step boration, oxidation, and nitration process, where BNNS was grown on Rh/Y stabilized zirconia (YSZ)/Si (111) substrate, $B(OCH_3)_3$ and NH_3 were used as the B and N sources, respectively [99]. Table 1 summarizes some common precursors, the related growth parameters, and the quality of the resulting BNNS.

Table 1: Precursors used to grow BNNS through the CVD process.

Precursor	Quality of the BNNS	Growth Conditions	Ref.
Ammonia borane	Single crystalline BNNS with domain size up to centimetre size was obtained. Mono- to multi-layers have been grown on various substrates.	Growth temperature varies from 700 to 1100 °C. APCVD and LPCVD systems are often used.	[18,20,21,44,56,65,85–88,92,100–124]
Borazine	Monolayer and few-layered BNNS have been achieved. Monolayer with domains as large as 0.3 mm has been reported.	UHV-CVD, LPCVD, and conventional APCVD systems have been used. Growth temperature varies from 700 to 1000 °C	[4,114,125–133]
β-trichloroborazine	Monolayer on Ni (111) and Pt (111) substrates was achieved.	Growth was carried out using a UHV system at 723 °C.	[40,84]
Diborane and ammonia	BNNS thickness (monolayer to 100-layers) and crystallinity are dependent on the choice of substrates, deposition time, and sequential exposures of the precursors.	Growth was carried out in an LPCVD system at 600-1025 °C.	[97,134]
Decaborane and ammonia	Thickness was about 2 nm on Ni and 2-15 nm on Cu	Growth was carried out at 1000 °C for 10 minutes in an APCVD system.	[98]
Dimeric diborazane and trimeric triborazane	Thickness was about 2-5 nm. Compared to ammonia borane, these precursors led to faster growth rates and more polymeric particles.	The precursors decompose around 80-90 °C. The growth was carried out at 1040 °C in an APCVD system.	[135]
BCl_3, NH_3, N_2, and H_2	The maximum thickness was about 10 nm	Growth temperature was 1000 °C in an APCVD system.	[96]
BF_3, N_2, and H_2	1-8 layer thick and a domain size of up to 4 μm were obtained	Microwave plasma CVD system was used for the growth. The microwave power, growth tempeature, and time was 800 W, 800 °C, and 1 hour, respectively	[93,94]
Trimethylamine Borane	Monolayer *h*-BN and *h*-BCN films were grown on Cu. With a sublimation temperature above 40 °C, 2-5% carbon doping can be achieved.	Growth was carried out at 1050 °C for 5-20 minutes using an APCVD system	[136]
Trimethylborate, O_2, and ammonia	*h*-BN monolayer	Growth was carried out in a three step boration-oxidation-nitration process in a LPCVD system.	[99]

4.2.3. Substrates for BNNS synthesis

The growth of BNNS has been carried out primarily on transition metal substrates due to their catalytic effect at high temperatures (Table 2). BNNS growth has also been reported on Ge [115], sapphire [79,103], Si [104], and SiO$_2$ coated Si substrate [108] (Table 2).

Similar to graphene, the most widely used substrates for BNNS growth are Cu and Ni. BNNS are reported to be strongly chemisorbed on Ni (111) and weakly chemisorbed/physisorbed on Cu (111) surfaces [137–139]. This is due to the strong hybridization of the Ni d_z^2 orbital with N-p_z and B-p_z orbitals, while in the case of Cu, the hybridization energy is much lower due to the filled d orbitals in Cu [137,138]. Thus, the binding energy between BNNS and Cu, Ag, and Au substrates is smaller than in the case of Co, Ru, and Ir. Theoretical calculations suggest that the binding energy decreases with the filling of the d band orbitals in transition metals and is the highest for the 4d elements (i.e., Period 5 elements) [138].

Table 2: Substrates for the CVD growth of BNNS in the context of the Periodic Table.

Period	Group								
	6	7	8	9	10	11	12	13	14
3								*Sapphire [79,103]	Si [104,111], *SiO$_2$ coated Si[108]
4	Cr [140]		Fe [125,126, 129,141]	Co [116]	Ni [4,5,40,97,100,120,128,142]	Cu [19,20,56,65,85,86,98,100,117,122] *Cu-Ni(5-30 at%) alloy [87],			Ge [115]
5			Rh [99,127]	Ru [119,121,143]	Pd [144]	Ag [132]			
6				Ir [130]	Pt [84,88,92]	Au[145]			

The positions of B and N atoms on the Ni (111) surface were theoretically analysed [146]. B atoms preferentially enter into the face centred cubic (f.c.c) or hexagonal close packed (h.c.p) hollow sites of Ni (111), and N sits on

top of each Ni atom for the formation of stable h-BN on top of Ni (111) [138,146]. The f.c.c position is energetically slightly more favourable for B atoms than the h.c.p hollow sites (energy difference is 9 ± 2 meV/B atom in the two sites) [146]. In a later publication, the stable B and N atomic positions on Co (0001), Ni (111), Pd (111), Pt (111), Cu (111), Ag (111), and Au (111) were established [139]. For the rest of the transition metals (Pd, Pt, Ag, and Au), B and N atoms sit on the bridge sites, and one of each sits on top of the transition metal atom alternatively to form stable h-BN (Figure 5a).

The lattice mismatch of Co (0001), Ni (111), and Cu (111) with h-BN is only 0.8%, -0.4%, and 2.4%, respectively (lattice spacing of Co (0001) = 0.251 nm, Ni (111) = 0.249 nm, Cu (111) = 0.256 nm, and h-BN = 0.250 nm). This facilitates commensurate epitaxial BNNS growth on these surfaces. There is a considerable lattice mismatch between h-BN and all the other transition metals, thereby forming non-commensurate corrugated nanomesh patterns. The Moiré periodicity generated by the lattice mismatch between the substrate and BNNS is calculated according to this formula [138]:

$$N_{BN} \times A_{BN} = N_{subs} \times A_{subs} \quad \text{...} \quad \text{(Eq. 3)}$$

Where, N_{BN} = No. of unit cell repetitions in h-BN

N_{subs} = No. of unit cell repetitions in the substrate

A_{BN} = Lattice parameter of h-BN

and A_{subs} = Lattice parameter of the substrate

For example, Ru (111) and Rh (111) have almost the same in-plane lattice parameter, 0.271 nm and 0.270 nm, respectively. From Equation (3), it can be estimated that 13×13 unit cells of h-BN coincide with 12×12 unit cells of Ru (111) or Rh (111). Therefore, the Moiré periodicity of the BNNS grown on Ru (111) or Rh (111) substrate will be the length of the 13×13 unit cells of BNNS. h-BN is normally more strained on the non-commensurate surfaces than on the commensurate ones (Figure 5b).

EBSD analysis has been carried out to understand the impact of grain orientation on the growth of BNNS [100,120,147–149]. Both the Cu and Ni substrates undergo a significant recrystallization when annealed at very

high temperatures (at or above 1000 °C), and the surfaces are found to be predominantly Cu(100) and Ni(100) oriented after the annealing and BNNS growth [120,147,150]. In all the studies, the BNNS growth rate was found to be higher on Cu(111) surfaces than on Cu(100) or Cu(110) [147]. The growth of BNNS on Ni, however, was found to be higher on Ni(100) or Ni(100)-like surfaces [120,149]. It should be noted that Cu(111) and Ni(111) have lower surface energies than their corresponding (100) and (110) surface planes.
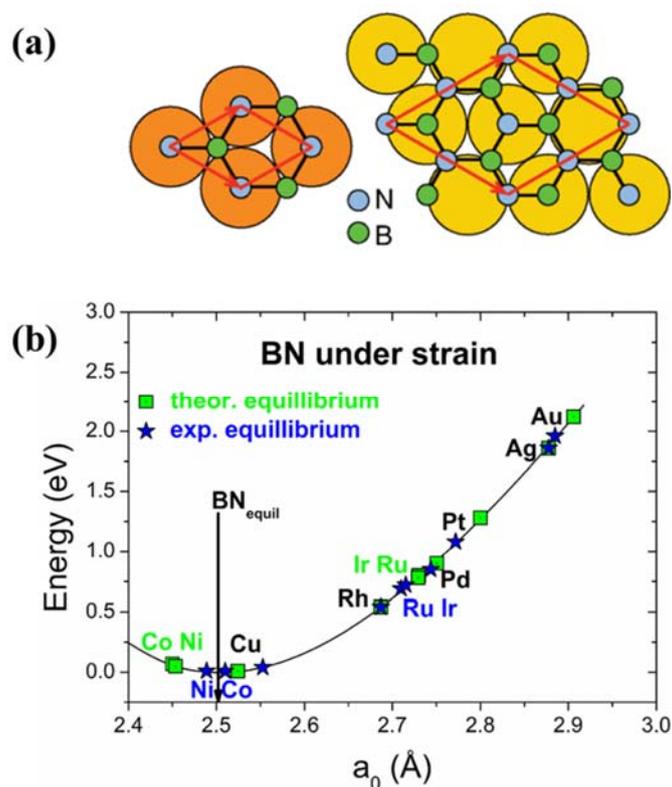
Figure 5: (a) Representative atomic positions of B and N in a stable *h*-BN monolayer sheet on Co (0001), Ni (111), Cu (111) (Left image, 1×1 *h*-BN unit cell on top of a 1×1 metal surface cell), and on Pd, Pt, Ag, and Au (111) (Right image, 2×2 *h*-BN unit cell on top of a √3×√3 metal surface cell). Adapted with permission from ref. 139. Copyright 2014 American Physical Society. (b) Energy vs lattice parameter plot, comparing equilibrium *h*-BN energy with *h*-BN sitting on (111) oriented transition metals. Adapted with permission from ref. 138. Copyright 2008 American Physical Society.

In a very recent study, multi-layered BNNS with centimetre-sized domains has been grown on Ni (111) single crystal [124]. Due to the high costs of single crystal, however, polycrystalline Cu, Ni, and Pt have been used, with

the aim of growing highly crystalline mono- and few-layer material [88,92,98,114,120,151]. As a result of the weak chemisorption and the polycrystalline nature of the substrate, triangular BNNS islands with random orientations are often found during the initial growth stage on polycrystalline Cu and Pt [44,86,88]. Moreover, triangular BNNS islands with different orientations within the same Cu grain have been observed, which is likely to be due to the weak interaction of the BNNS with the Cu substrate [86]. In contrast, BNNS islands grown on Ni and Ru substrates maintain specific orientations with respect to the substrates due to the strong chemisorption of BNNS on those substrates [40,121].

4.2.4. Pre-treatment of the substrate

Commercially available high purity (>99.9 % purity) polycrystalline thin film (0.025 mm to 0.25 mm) foils are generally used to synthesize BNNS. These as-received foils normally need treatment prior to the growth to remove the oxide layer and organic contaminants. A short acetic acid wash has been found to be effective to remove the oxidized layer from the Cu surface [122]. Acetone and isopropyl alcohol (IPA) are used to remove any organic contamination [152]. Another widely used technique is to treat the Cu or Ni foils in dilute nitric acid for a very short period to remove the oxidized layer and contaminants [56,106]. Electrochemical polishing and Ar ion etching are the other alternatives for polishing the foils before the growth [153–157].

On the polycrystalline Cu substrates, the presence of grain boundaries and other defects often lower the lateral size and homogeneity of the nanosheet [65]. Electropolishing can minimize the defects on the Cu surface [44], although the presence of Cu grain boundaries and preferential BNNS growth along those lines are apparent (Figure 6a). Long annealing of the Cu substrate at high temperatures can facilitate the growth of single crystal BNNS with lateral sizes up to 20 micrometers (Figure 6b) [21]. The lateral size of up to 130 μm could be obtained when the growth was carried out on Cu-Ni foil (85:15 at. %) (Figure 6c) [87]. Melting the Cu substrate has been found to be an effective method to reconstruct the surface, and micrometer-sized and mostly 1-2 layered BNNS have been obtained (Figure 6d) [65]. Extensive cracking of the BNNS was found when the growth was carried out on the melted Cu substrate (Figure 6e, f). Flattening the Cu substrate against the tungsten support (to ensure good contact between the two metals) consequently improves wetting during melting and minimizes temperature gradients across the foil. Slow cooling through the Cu melting point and eliminating the presence of SiO_x particulate contaminant that can etch the nanosheet, lead to improved BNNS growth on melted Cu (Figure 6g, h)

[49]. Also, re-solidifying the Cu substrate and carrying out the growth at temperatures near the melting point was reported to facilitate growth [117].
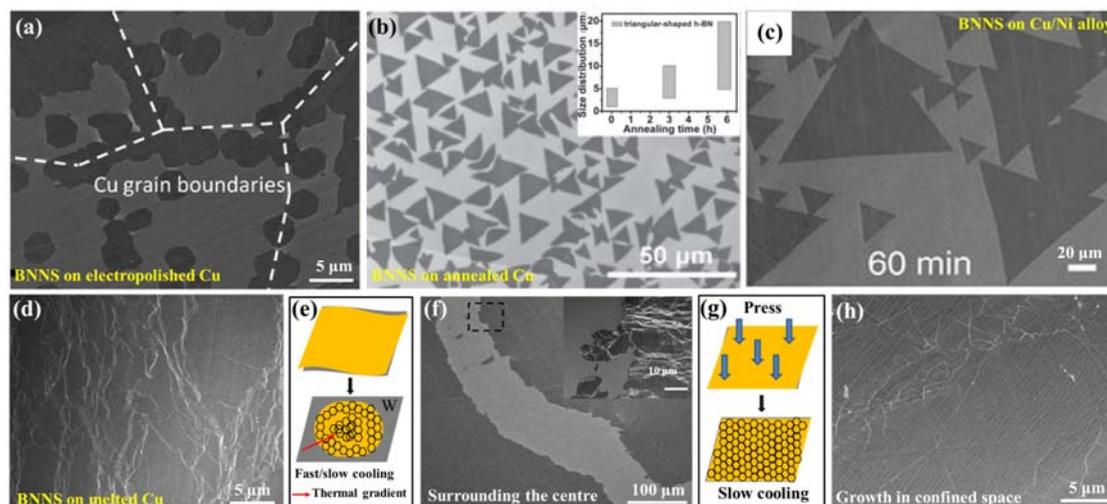

Figure 6: Impact of substrate morphology on the growth of BNNS. (a) BNNS grown on electropolished Cu substrate at 1050 °C. Preferential BNNS growth along the Cu grain boundaries is apparent. Adapted with permission from ref. 44. Copyright 2014 American Chemical Society. (b) Cu substrate annealed at 1000 °C improves the crystal size of the BNNS. Inset is a plot of size of the BNNS vs annealing time. Adapted with permission from ref. 21. (© 2014 WILEY-VCH Verlag & Co. KGaA, Weinheim). (c) BNNS grown on CuNi (85:15) alloy at 1085 °C. Adapted with permission from ref. 87. Copyright 2015 Nature Publishing Group. (d) Melting the Cu substrate facilitates homogenous BNNS growth. Large crumples in the sheet are apparent from the SEM image. Adapted with permission from ref 65. Copyright 2015 Nature Publishing Group. Schematic illustrations of (e) an unflattened and (g) a flattened Cu substrate and the resultant re-solidified Cu shape after melting. SEM images of BNNS grown on (f) unflattened (inset: higher magnification) and (h) flattened Cu substrates. Minimizing the thermal gradients across the Cu and BNNS during cooling and carrying out the growth in a SiO$_x$ particle-free environment facilitates the growth of crack- and crumple-free BNNS. Reproduced from ref. 49 with permission from The Royal Society of Chemistry.

4.2.5. Mechanism of BNNS growth

For precursors such as ammonia borane, NH_3 and B_2H_6/$B_{10}H_{14}$, borazine is formed and adsorbed on the catalyst surface, where it polymerizes and ultimately forms BNNS on the substrate surface via the dehydrogenation

reaction at high temperatures [19,128,158]. Borazine can decompose into boron and nitrogen when it comes into contact with the substrate [131]. B has sufficient solubility in Cu at high temperatures (0.29 at% at 1013°C [159]), while N atoms are expelled from the surface due to their low solubility in Cu. Initially boron and nitrogen form monolayer BNNS on the substrate (Figure 7a). B atoms, which diffuse towards the surface can combine with N, forming multilayer islands of BNNS [126,131]. It is also found that by 'pre-filling' Fe substrate with N atoms (flowing NH_3 at the beginning of the growth), the diffusion of B atoms from the decomposed borazine can be restricted, and island-free, uniform monolayer growth of BNNS can be obtained [126].

The growth of multilayered BNNS is often explained by three established thin film growth models (Figure 7b) [5,86,119,122,160,161]. If the atoms of the deposited material are much more strongly bonded to each other than to the substrate, island or Volmer-Weber growth takes place (case 1: Figure 7b). In contrast, if the atoms are more attracted towards the substrate, the growth occurs in a layer-by-layer manner, i.e., the growth follows the Frank-van der Merwe model (case 3: Figure 7b). The third one is the Stranski-Krastanov growth model, where the growth follows the Frank-van der Merwe model first (layer-by-layer growth), and after that, the growth switches towards the island-like growth (case 2: Figure 7b). Most BNNS growth has been explained by the Stranski-Krastanov model [5,86,119,122].
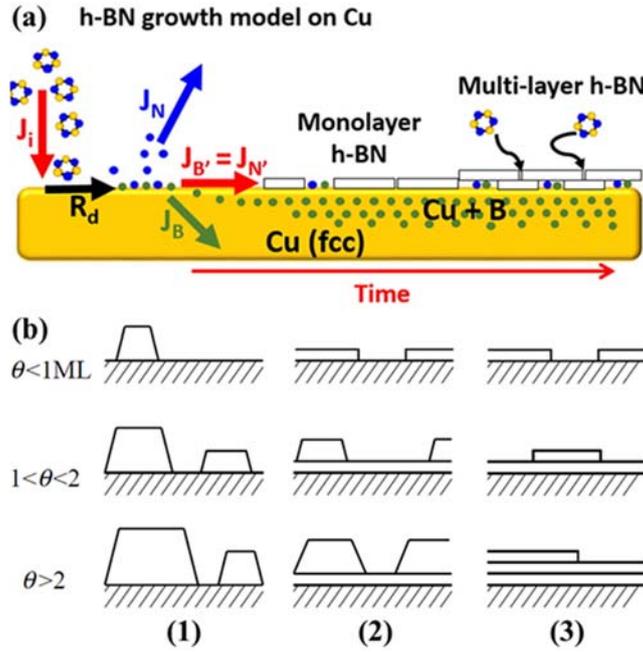
Figure 7: Schematic illustration of BNNS grown on Cu by the CVD process. J_i is the impingement flux of borazine, J_B is the diffusion flux of B into the Cu substrate, J_N is the diffusion flux of N out of the Cu substrate, and $J_{B'}$ and $J_{N'}$ are the flux of B and N atoms to form h-BN on Cu. Reproduced with permission from ref. 131. Copyright 2014 American Chemical Society. (b) Three thin film growth models that are often used to explain BNNS growth, as a function of coverage and the thickness, θ, in monolayers: (1) Volmer-Weber, (2) Stranski-Krastanov, and (3) Frank-van der Merwe growth models. Adapted with permission from ref. 161. Copyright 2000 Cambridge University Press.

4.2.6. Transferring BNNS to various substrates

Transfer of the CVD grown BNNS onto various metal substrates has been achieved with supports such as poly(methyl methacrylate) (PMMA) and polydimethylsiloxane (PDMS), thermal release tape, and water soluble polymers [56,86,128,162–168]. PMMA is the most widely used polymer to transfer the nanosheet [19,56,128,169]. As the deposition occurs normally on both sides of the substrate, one side of the substrate is first cleaned using either acid etching or Ar ion sputtering. PMMA is then spin-coated on the other side of the substrate and the underlying metal is etched away in $FeCl_3$ [19,85,98,170], $Fe(NO_3)_3$ [171], Transene Cu etchant solution [19,114], or ammonium persulfate [172] solution. The free floating BNNS/PMMA is then collected on a silicon wafer for subsequent analysis. The PMMA can be dissolved by washing with hot acetone followed by Ar/H_2

19

annealing at 350-450 °C for 2-4 hours, to leave the free-standing BNNS layer. This transfer process, however, often leaves PMMA residue all over the sample. Heating at 500 °C under Ar/O$_2$ gas atmosphere has been found effective for complete removal of PMMA residues from the BNNS [173]. Also, the acetone washing step can be replaced by oxidising the PMMA coated sample in air at 350 °C for 3-4 hours, immediately after collecting it from the solution [174]. Oxidising the PMMA layer saves several steps and can avoid any unwanted contamination from residual organic material. In a recent work, electrostatic force has been used to transfer graphene from the Cu substrate using an electrostatic generator [168]. Similar methods may be adopted for transferring BNNS. In addition, directly transferring BNNS to a TEM grid has also been achieved, similar to the method adopted for graphene transfer [165]. In this process, the TEM grid is kept on top of the BNNS/Cu foil and a few drops of IPA are added, so that the TEM grid adheres to the BNNS/Cu foil. After etching the underlying Cu, BNNS sticks to the TEM grid and floats on the etching solution [117,165,175].

4.3. Physical vapor deposition (PVD)

PVD is another bottom-up synthesis process, where materials are vaporized from a solid or liquid source in the form of atoms or molecules and are transported towards a substrate under UHV or a low-pressure gas (plasma) environment for deposition [176]. The vapour from the source materials is normally generated by two techniques: thermal evaporation and sputtering. In the thermal evaporation process, the source material is heated up by a focused high energy electron beam to vaporize the material. Molecular beam epitaxy, a PVD process, is based on an advanced form of thermal evaporation. Sputtering is generally carried out by bombardment of the source material using accelerated gas ions (typically Ar$^+$). Ar+ ion sputtering of a pure *h*-BN target has been employed to grow mono- to few-layer BNNS on Cu and Ni substrates [177–179]. Radio frequency magnetron sputtering was employed on a B target at 850 °C in Ar/N$_2$ atmosphere to synthesize monolayer BNNS on Ru (0001) [143]. Pulsed laser deposition (PLD) was also employed for synthesizing BNNS on various substrates, including Ni, Mo, Si, and AlN [180].

4.4. Other processes

Apart from the conventional bottom-up or top-down approaches, BNNS has been synthesized by substitutional reaction of graphene [181–184]. To synthesize the nanosheet, boron trioxide powders, molybdenum oxide (as a

promoter), and graphene sheets, were put into a graphite furnace at 1650 °C under N_2 gas [181]. Both BN and BCN nanosheet have been synthesized in this way. Modification of the process by using diverse carbon sources (for example, fleabane flowers, pine needles, wiper papers) resulted in gram scale amounts of BNNS [185]. Porous BNNS, which was used for CO_2 adsorption, was synthesized by flowing ammonia gas over MgB_2 and NH_4Cl powders at about 650-850 °C in a CVD furnace [186]. A mixture of boron trioxide and guanidine chloride in methanol was also used to produce porous BNNS at 1100 °C [187]. We have reported a simple method to exfoliate and functionalize BNNS in a moisture-rich environment at about 850 °C [188]. The high temperature oxidation produces B-OH groups along the edges, which helps effective crosslinking with the hydrogel polymer to increase its thermal response [188].

4.5. Challenges in BNNS synthesis

Although several synthesis routes have been identified to yield mono- and few-layer BNNS, the production of large and single-crystalline nanosheet with controlled thickness for practical use is still a challenge. The top-down approach normally leads to BNNS with various thicknesses and lateral sizes, and contamination due to the chemicals used. Using the mechanical cleavage technique, nano- to micrometer sized BN flakes can be peeled off from a pristine highly oriented pyrolytic boron nitride sample. This process has a low yield; however, both mono- and few-layered nanosheet were produced by this method. In sonication assisted exfoliation, defective and small-sized nanosheet are often found.

Electron beam irradiation and PVD methods require complex fabrication systems, and typically only laboratory-scale production is possible with them. Other processes, such as boron nitride nanotube (BNNT) unwrapping and the substitution reaction of graphene, produce nanosheet which are neither of high purity nor large in size. Variable thicknesses and impurities are the main drawbacks of the wet chemical routes. The as-synthesized nanosheet may also require a high-temperature anneal (1000-1500 °C) to improve their crystallinity and sometimes require oxidation to remove the carbon contamination [25,181].

As far as BNNS as a substrate for 2D nanoscale electronics is concerned, among the various synthesis routes, the CVD method has been deemed to be an effective route to produce large BNNS for practical applications. Recently, graphene layers, 30 inches in length, were synthesized by a CVD method and then transferred using a

roll-to-roll technique [167]. Large BNNS (25 inch in length) have recently been grown on a rolled Cu substrate [189]. The major challenges for the CVD growth are how to minimize the grain boundaries (in the other words, to grow larger single crystals) and how to control the formation of mono- or few-layers (that is, homogeneity) over a large area. Carbon and silicon oxide contamination in the CVD grown BNNS have been reported ([49]). The precursors for BNNS need to be free of any residual solvents to avoid carbon contamination, and growth in a confined space has been found to minimize the contamination by silicon oxides. Also, effective methods for transferring BNNS to various substrates need to be developed to avoid breakage and contamination during the process.

5. Characterization techniques

Due to its few-layer nature, BNNS requires somewhat special knowledge for investigating its morphology, crystallinity, number of layers, and overall quality. In the following section, we summarize the recent progress in the characterization of BNNS, from electron microscopy to spectroscopy. Some of these techniques can be adopted to characterize other 2D materials.

5.1. Optical microscopy

Mono- to few-layer BNNS cannot be easily observed in an optical microscope, as h-BN hardly absorbs any visible light (being nearly transparent) due to its large band gap (about 6.0 eV). Even using a very smooth 300 nm SiO_2/Si wafer to increase the interference of reflected light does not add sufficient contrast to observe a monolayer. Monolayer BNNS results in 1.5% contrast (which comes from the difference in optical path between the incident and reflected light) under white light on 300 nm SiO_2/Si, which is undetectable by the human eyes [190]. The contrast difference increases to 2.5 % for monolayer h-BN on top of 80 nm SiO_2/Si wafer under white light, and 3.0 % using a green light (Figure 8a) [190]. With an increasing number of layers, the optical contrast increases. One study of 1-80 layers of h-BN showed a monotonic increase in contrast with layer number under green light illumination (516 nm wavelength) [191].

Spin coating liquid crystals (4-pentyl-4′-cyanobiphenyl (5CB), 4-octyl-4-cyanobiphenyl (8CB), etc.) on top of BNNS has proven to be helpful for directly identifying the grains and cracks in BNNS using polarized optical

microscopy (POM) imaging [114,148,192]. The method was first used for graphene [193,194] and later on applied to BNNS [114,148,192]. Liquid crystals have been found to be aligned anisotropically along the domain boundaries of BNNS and exhibit distinct birefringence when imaged under polarized light (Figure 8b-d) [148,192]. The grain boundaries of the growth substrate (Cu), however, result in residual morphology in the BNNS after transfer [114,193], which can be confused with BNNS grain boundaries.

BNNS can be identified directly on the Cu substrate under an optical microscope after oxidizing the Cu substrate at about 200 °C for a few minutes [135]. The oxidation increases the interference contrast between the oxidized and non-oxidized Cu substrate, which facilitates the direct identification of BNNS areas. This method was also first used on graphene-coated Cu substrate [195].
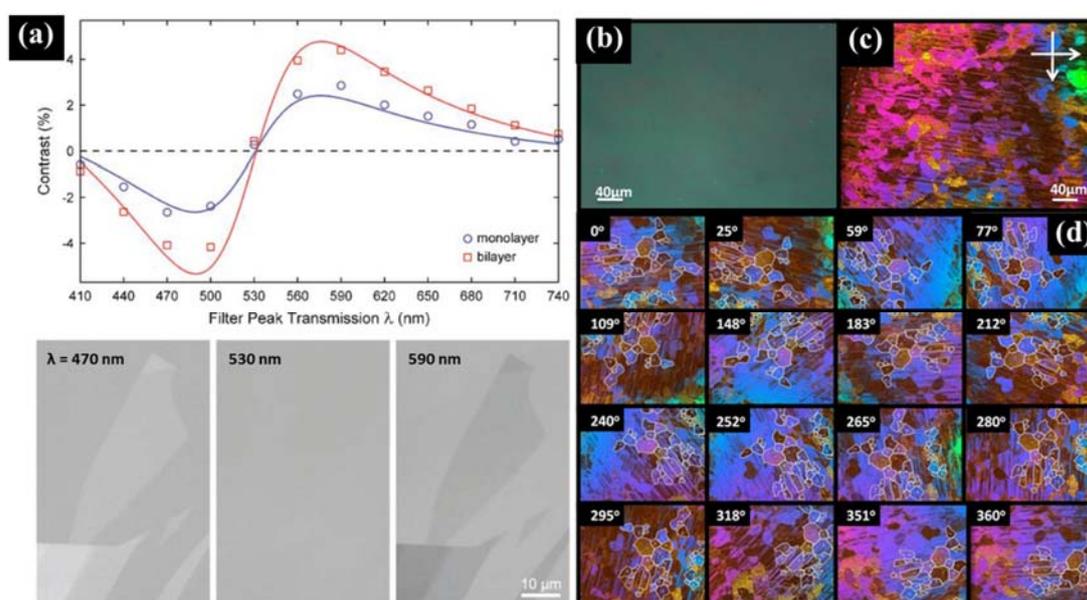
Figure 8: (a) Optical contrast change of mono- (blue line) and bi-layer (red line) region with different wavelengths of light. The positive contrast maximum is at about 570 nm wavelength. The bottom panels of (a) show the contrast variation of mono- and bi-layer h-BN under different wavelengths of light. Reproduced with permission from ref. 187. (© 2011 WILEY-VCH Verlag & Co. KGaA, Weinheim). (b-d) Liquid crystal helps in the direct identification of BNNS domains on Cu substrates. (b) BNNS on SiO_2/Si wafer and (c) cross-polarized optical microscope (POM) image of BNNS after coating with liquid crystal. (d) POM images as a function of polarising filter rotation angle. Adapted with permission from ref. 189. Copyright 2015 Nature Publishing Group.

5.2. Raman Spectroscopy

Crystalline h-BN shows two Raman active E_{2g} peaks [196–199] at 1366 cm^{-1} and 49-52.5 cm^{-1}. The peak at 1366 cm^{-1} is due to the B and N atom stretching vibrations, while the other peak arises when the h-BN planes slide against each other [199]. The appearance of the high frequency E_{2g} Raman vibration mode is the most straightforward route to detect h-BN. Monolayer h-BN gives a very weak Raman E_{2g} band. With an increasing number of layers, the Raman peak intensity increases proportionally. Gorbachev et al. [190] identified mono-, bi-, and few-layer BNNS by Raman spectroscopy. The Raman peak of monolayer BNNS was blue shifted up to 4 cm^{-1} and was observed at 1370 cm^{-1}. It was inferred that the monolayer h-BN was stretched by the underlying substrate, which develops strain in the nanosheet and consequently hardens the E_{2g} phonons. In the bi-layer and few-layer cases, a red shift of 1-2 cm^{-1} was found. This could be due to the interaction between neighbouring sheets, which can soften the E_{2g} phonons [190]. Heat generated from the high-intensity laser source can also soften the phonons in the presence of defects in the nanosheet and produce a red shift in the Raman peak. Defects such as vacancies and impurities restrict the heat flow, and therefore, the temperature can rise in the defective areas, which softens the E_{2g} peak.

5.3. Fourier transform infrared spectroscopy (FTIR)

FTIR is an important tool for analysing boron nitride. An attenuated total reflectance (ATR)-FTIR arrangement is often used to analyse thick BNNS samples directly or in liquid solvents [89,180,200–202]. FTIR is not very sensitive, however, for detection of mono- to few-layered BNNS on 300 nm SiO_2/Si substrate. *h*-BN has two characteristic infrared (IR) modes. One is the in-plane B-N stretching vibration, E_{1u}, within the range of 1366-1392 cm^{-1}, and the other is the out of plane B-N-B bending vibration, A_{2u}, at 770-820 cm^{-1} wavenumbers [200,202].

5.4. Scanning electron microscopy (SEM)

Due to its minimal sample preparation requirements and its capability for imaging micro- to nanoscale areas with

24

high resolution, ease of use, and non-invasiveness, SEM is another commonly used characterization tool. The identification of BNNS, however, necessitates a conducting substrate, low operation voltage, and short working distance. Mono- to few-layered BNNS is considered transparent under high kV electron beam operations in SEM, as the interaction volume and the secondary electron generation from the nanosheet are very low compared to the substrate. Thus, the surface underneath the BNNS is imaged under high kV SEM operation. Also, BNNS is difficult to identify on top of insulating substrates (i.e., SiO_2/Si). This is due to the charge built up on the insulating surface under electron beam irradiation, which repels further incident electrons and restricts the secondary electron generation. With an increasing number of layers, SEM contrast increases proportionally [203].

5.5. Transmission electron microscopy (TEM)

This technique can be operated in either broad beam illumination mode (conventional TEM), or the beam can be focussed to a fine probe and scanned (scanning TEM – STEM), in a manner analogous to SEM. The crystallinity of the BNNS is generally examined by selected area electron diffraction (SAED) analysis in TEM [49,56,65,125,128,141,204]. The appearance of six-fold symmetrical spots in the SAED pattern confirms the presence of crystalline BNNS. Various domains of the nanosheet can be sequentially imaged under dark field (DF)-TEM mode by selecting specific SAED spots with an objective aperture [174,205]. The overall domain boundary distribution can be obtained by grouping all the DF images together. The domain size analysis of the BNNS has been reported using this DF-TEM technique (Figure 9a, b) [49,204].

The thickness of the BNNS is conventionally determined by counting individual atomic layers at folded edges of the sheet in high resolution TEM (HRTEM) images. The atomically thin sheet can be folded along the edges during the transfer step. The creases in the sheet can be also detected under similar HRTEM analysis [206]. The serendipity of getting a folded edge and the presence of creases, however, often makes it challenging for accurate identification of the thickness across all the regions.

High-angle annular dark field (HAADF)-STEM is a good technique to identify the individual atoms and the layer thickness, based upon HAADF intensity, which varies with the atomic number (Z) (in the relation of $Z^{1.64}$) [207]. The precise identification of thickness by annular dark field (ADF)-STEM imaging, however, is a tedious process as it requires the presence of a background (a hole, created by electron beam irradiation damage to BNNS) as a

25

reference.
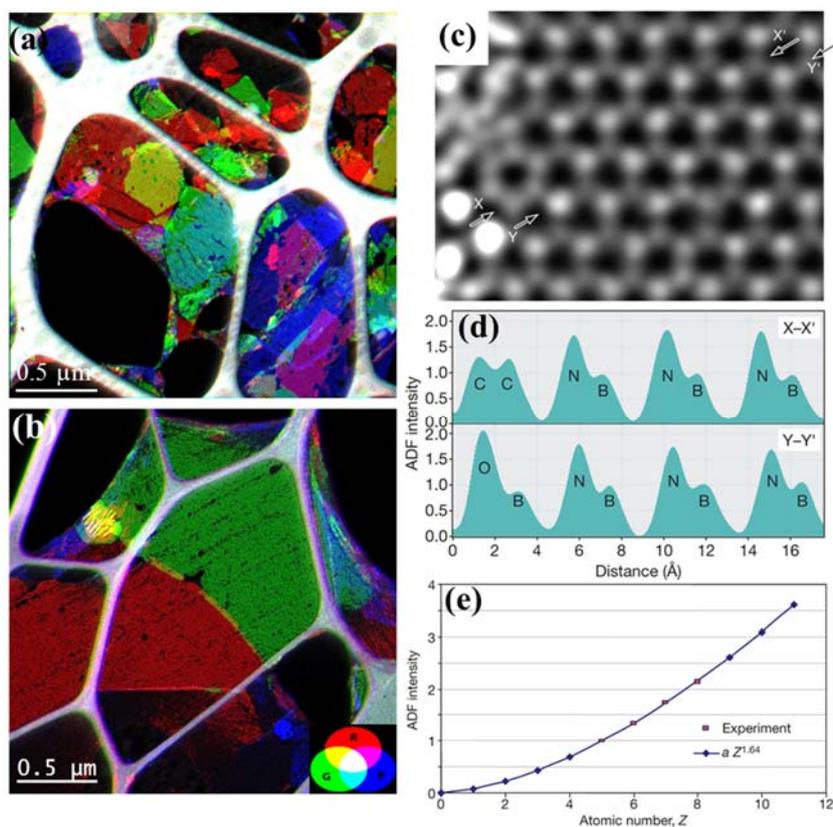
Figure 9: (a-b) Colour-coded combined DF-TEM images to analyse domain sizes of BNNS. (a) Multilayered and few hundred nanometer-sized BNNS domains grown on a solid Cu substrate can be observed, while (b) large (micrometer-sized) BNNS domains are found on a melted Cu substrate. Inset of (b) is the RGB colour image. Adapted from ref. 49 with permission from The Royal Society of Chemistry. (c) HAADF-STEM image of monolayer BNNS, and (d) the corresponding intensity profiles along the XX′ and YY′ directions. Impurity elements, i.e., C and O, in the nanosheet can be identified from their relative intensities. (e) The ADF intensity vs. atomic number (Z = 1 to 11) plot gives a perfect match for the B, C, N, and O intensities between the experimental and theoretical values. Adapted with permission from ref. 205. Copyright 2010 Nature Publishing Group.

HAADF-STEM is a powerful tool for identifying individual atoms, defects, and grain boundaries in BNNS. The individual B and N atoms and the impurity atoms inside the BNNS have been successfully detected by HAADF-STEM analysis (Figure 9c, d) [208]. The experimental HAADF intensities from the B, C, N, and O atoms match the theoretical profile line (Figure 9e) [208].

The nature of the bonding (sp^2 or sp^3 configuration) and the chemical constituents can be analysed by electron energy loss spectroscopy (EELS). TEM-based EELS is very effective for the characterisation of low atomic weight elements (from Li to 3d transition metals) [209], while TEM-based energy dispersive X-ray spectroscopy (EDS) is more sensitive for higher atomic number elements, although newer generation detectors allow good sensitivity for C and all heavier elements. EELS and EDS mapping are frequently conducted to analyse the spatial distribution of elements. The advantage of EELS over EDS is the much higher energy resolution of the former (~ 1 eV vs. 130 eV, respectively). This higher energy resolution in EELS allows the measurement of chemical shifts and fine structure within the energy loss edge. This provides a very sensitive probe of atomic bonding effects. Therefore, EELS permits both the composition and the bonding configuration to be determined. High resolution (HR)-EELS analysis has been also employed to identify the defects in the BNNS [210]. In addition, it has been theoretically suggested that various stacking orders in the BNNS will give rise to changes in B and N K-edge EELS, which can be useful in identifying the exact stacking orders [211].

5.6. Atomic force microscopy (AFM)

AFM is a versatile characterization instrument for 2D materials. The topography of the BNNS sample can be accurately measured, generally under tapping mode in AFM. For the mono- and few-layer cases, precise layer number determination under AFM can be challenging, however. Often a thickness of 1 nm can correspond to monolayer BNNS (since the interlayer spacing of h-BN is 0.333 nm), due to the trapped molecules between the nanosheet and the SiO$_2$/Si substrate [212,213]. Therefore, other characterization techniques, such as optical, Raman, SEM, and TEM/STEM analysis are required to correlate with the AFM-derived thickness.

The mechanical strength of few-layer BNNS has been determined using the AFM indentation technique (Figure 10) [56]. A circular hole 1 μm in diameter was first created in a SiO$_2$/Si surface by e-beam lithography or reactive ion etching. The nanosheet was then transferred to the SiO$_2$/Si surface, and a diamond tip was used to indent the free-standing nanosheet to determine the fracture strength.
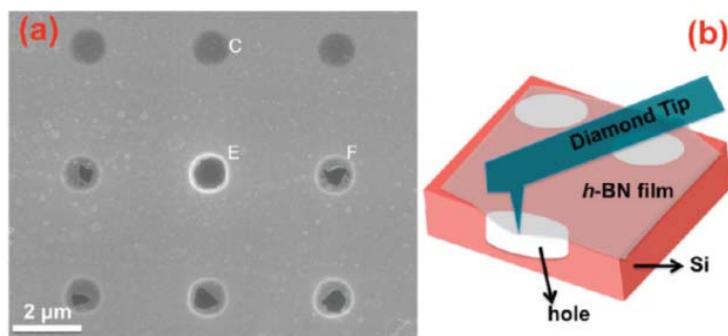
Figure 10: Determination of the mechanical strength of BNNS by the AFM indentation technique. (a) SEM image of large BNNS on a SiO$_2$/Si substrate, with a patterned array of circular holes in the substrate. Areas C and E are fully covered by BNNS, and area F is the region fractured by indentation. (b) Schematic illustration of mechanical strength determination by nanoindentation. Reproduced with permission from ref. 56. Copyright 2010 American Chemical Society.

The quality of BNNS has also been determined by conductive AFM analysis in contact mode [214]. BNNS is generally considered as an insulator due to its wide band gap, although the presence of impurities and defects in the nanosheet will increase its conductivity. This can be used as a metric of quality of the sheet under conductive AFM. Frictional characteristics of mono- to multiple-layer 2D nanosheet was examined in friction force microscopy and contact mode AFM analysis [215]. Friction increases with a decreasing number of layers, which was ascribed to the puckering characteristics of the thin nanosheet under AFM tip sliding.

5.7. X-ray photoelectron spectroscopy (XPS)

XPS analysis is generally performed directly on the growth substrate before transferring. Identification of the elements, their quantity, and their oxidation state can be derived from the XPS spectra. The presence of B and N has been identified at 190.3 eV and 398.8 eV, respectively [56,74,92,96,100,120,128,132,216–218]. Two small broad peaks also can appear at energies of 9 eV and 25 eV (plasmon and bulk plasmon loss peaks) higher than the B 1s and N 1s core level peaks, respectively, which is a fingerprint signature of the sp^2 bonding between B and N atoms [31,219]. For amorphous and cubic BN samples these peaks do not appear.

5.8. Ultraviolet-visible (UV-vis) spectroscopy

BNNS has poor absorption in the visible light range and therefore appears transparent under optical microscopy [190,220]. BNNS grown by the CVD process needs to be transferred to quartz plates for collecting the UV-vis spectrum. A sharp absorption peak can be observed at about 200 nm for BNNS [56], while *h*-BN bulk samples show the peak in the 215-227 nm range [221]. The band gap of few-layer BNNS has been determined by analysing the absorption data acquired by UV-vis spectroscopy, according to Tauc's formula [222],

$$\omega^2 \varepsilon = (h\omega - E_g)^2 \dots\dots\dots\dots\dots\dots\dots\dots\dots\dots\dots\dots\dots\dots\dots\dots\dots \text{(Eq. 4)}$$

Or, through this reaction:[223]

$$\alpha = C(E - E_g)^{1/2}/E \dots\dots\dots\dots\dots\dots\dots\dots\dots\dots\dots\dots\dots\dots \text{(Eq. 5)}$$

Here, ω = Angular frequency = $2\pi/\lambda$

α = Absorption coefficient, which can be obtained from $\varepsilon = \alpha L$, where ε is the absorption value and L is the film thickness.

       h = Planck's constant

       E_g = Band gap energy

       E = Incident photon energy

The Tauc's formula has been used, assuming that the BNNS has a direct band gap. In a recent publication, however, *h*-BN has been suggested to be an indirect band-gap material [224].

5.9. Other techniques

Scanning tunnelling microscopy/spectroscopy (STM/STS) analysis gives atomic scale information, in which individual atoms can be detected by atom-to-atom raster scanning. Square octagon pairs (4/8) and pentagon-heptagon pairs (5/7) were detected along the domain boundaries by STM [54]. Defects generated during the growth [121] and the periodicity of BNNS [121,139,225] grown on different substrates have been analysed by STM.

Auger electron spectroscopy (AES) can be employed to determine the B and N concentrations in BNNS as a substitute or a complement to XPS analysis [87,151,203,217]. In an *in-situ* study of BN doping of graphene, the B XPS signal for both 2 % and 6 % BN doping was not detectable due to the low atomic sensitivity [151]. In AES, however, both boron and nitrogen peaks are apparent [151].

High energy X-ray absorption spectroscopy (XAS) and X-ray emission spectroscopy (XES) under synchrotron radiation have been used to obtain a better understanding of the fine details of the B and N bonding and their interactions with the substrate [129,151,226]. Secondary ion mass spectroscopy (SIMS) has been used for depth profiling and elemental identification [31,125]. The crystallinity of the nanosheet has also been studied by low energy electron diffraction (LEED) analysis in a photoemission/low energy electron microscope (PEEM/LEEM) [227][129][228].

Single atomic defects in BNNS have been identified using photoluminescence spectroscopy [229]. BNNS is strong ultraviolet ray emitter [221,230], but spectral emissions in the visible range are seen in the presence of defects in monolayer or multilayer BNNS [231,232].

6. Properties and applications

6.1. Substrate for 2D nanodevices

The *sp²* bonded BNNS is atomically flat, insulating, and isostructural to graphene. The charge impurities and dangling bonds that are inherent to a silica substrate are completely absent in BNNS [17]. In addition, there are only weak van der Waals forces between graphene and BNNS. Therefore, by using BNNS as a substrate for graphene devices instead of SiO_2, the charge transport through graphene was improved significantly [17]. This fact has emphasised the necessity of making large-area crystalline BNNS and improving the transfer procedures to build BNNS-supported 2D hybrid structures. In recent reports, BNNS has been demonstrated as a dielectric layer for the fabrication of graphene-based field effect transistors (FETs) [19,107] and explored as a tunnelling barrier between graphene layers [233]. BNNS-supported flexible transistors have also been reported [70,234].

6.2. Chemical resistivity and corrosion protection

h-BN is inert to both strong acidic and basic solutions [76]. Due to its chemical inertness, it can hardly been functionalized [201], while its counterpart graphite can be easily converted to graphene oxide through the Hummers [235] and modified Hummers methods [236]. BNNS, with a pore diameter of only 1.2 Å in the hexagons [237], has been demonstrated to be impermeable to argon atoms [238]. Therefore, BNNS has good potential as a protective layer for nanoscale electronics, where the thickness and stability of the underlying substrate are crucial in harsh environmental conditions [214,239–241]. We have demonstrated that the use of high quality BNNS with large domains and a limited number of defects is essential for effective corrosion protection of the underlying Cu substrate in 0.5 M NaCl solution [204]. In the presence of only 1-2 atomic BN layers on Cu, the impedance value obtained from electrochemical impedance spectroscopy (EIS) is over one order of magnitude higher compared with that of the bare Cu substrate (Figure 11a, b). Optical microscope examination of the Cu surface before and after the EIS testing clearly reveals that the BNNS/melted Cu substrates are the least affected (Figure 11c-f). Multi-layered BNNS with a large number of defects, however, shows accelerated corrosion towards water [204]. Experimentally, fragmented BNNS on Cu is found to accelerate the underlying Cu oxidation in air and water at room temperature (Figure 11g-i) [204]. Also, along the BNNS edges, severe Cu oxidation was apparent (Figure 11g, h). From the density functional theory (DFT) calculations, dissociation of water into O* and 2H* is found to be most energetically favoured along the edges of BNNS in the presence of Cu substrate (Figure 11i). The B and O* interaction provides additional stability of the O atom on the Cu substrate, thus accelerating the Cu oxidation in the presence of BNNS.

*6.3. Mechanical stability and use as fillers in polymer composites*

The elastic modulus of 1-2 nm thick BNNS has been theoretically and experimentally determined (by the AFM nanoindentation technique) to lie in the range of 184 to 510 N/m [56,242], which is comparable to the performance of high strength steel, although much less than that of graphene (about 1000 N/m) [243]. The experimental bending modulus, however, is much lower (8.8-16 N/m for 1-2 nm thick BNNS) [56], compared to the theoretical value (31.2 N/m) [244], possibly because of the presence of a large number of defects in the CVD grown nanosheet.

The low density, high strength, and large elastic modulus of BNNS help to improve the mechanical performance of polymer composites. Several polymers, including poly(methylmethacrylate) (PMMA), polyvinyl acetate (PVA), and polybenzimidazole, have been studied separately as matrices, with exfoliated BNNS acting as fillers to improve the strength of the composites [245–249]. Good dispersion, their strength and wrinkles, and partial polarity in the B-N bonds were suggested as the possible reasons for the improvement in mechanical properties [247].

6.4. Thermal conductivity enhancer

h-BN has a highly anisotropic thermal conductivity, with its in-plane thermal conductivity calculated to lie within the 100-2000 W/mK range; while along the out-of-plane direction, the value falls to only a few W/mK [250–252]. The experimental value for 11-layer *h*-BN was reported to be 360 W/mK (390 W/mK for bulk *h*-BN) and 250 W/mK for 5-layer *h*-BN. The lower thermal conductivity in the few-layer BNNS is attributed to residual polymeric particles after the transfer process [253]. The high in-plane thermal conductivity and insulating nature of BNNS have been employed to prepare thermally conductive nano-oils containing BNNS nanofiller [254,255]. The thermal conductivity of BNNS has also been utilized in polymeric composites to make highly thermally conductive composites [245,247,249]. A 14-fold increase in thermal conductivity was observed in an electrically insulating epoxy/BNNS composite [185,256].
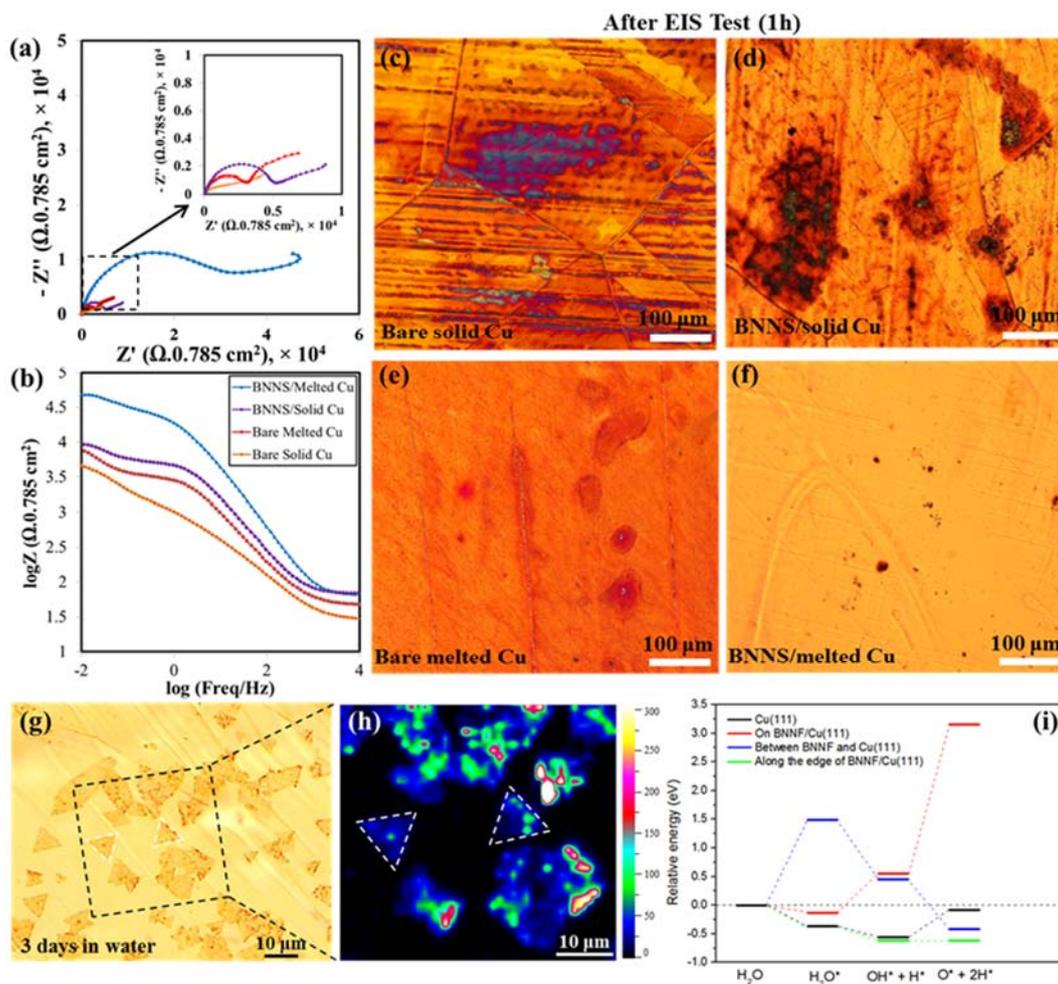
Figure 11: (a) Nyquist (inset: enlargement of high frequency region) and (b) Bode plot of bare and BNNS coated Cu samples. The BNNS/melted Cu sample, where BNNS has larger domains and fewer defects, shows highest impedance value among all the samples. (c-f) Optical images of bare and BNNS coated Cu substrates after the EIS test. BNNS/melted Cu substrate is seen to be the least affected after the EIS test. (g-i) Accelerated oxidation of Cu substrate underneath h-BN is observed after 3 days of water immersion. (g) Optical image of partially h-BN coated Cu substrate and (h) Raman mapping image in the 500-700 cm^{-1} wavelength range of the marked area in (g), suggesting more Cu oxidation areas underneath the h-BN cover. (i) Water dissociation energy diagram on Cu (111) surface. Adapted with permission from ref. 201. (© 2017 WILEY-VCH Verlag & Co. KGaA, Weinheim).

6.5. Sliding and frictional characteristics

The lamellar structure, weak van der Waals force interactions between the layers, strong in-layer bonding, high mechanical strength, chemical inertness, and stability from sub-zero to very high temperatures have made h-BN a popular lubricating agent on the bulk scale [257]. On the 2D scale, where the layer numbers are reduced from billions to a few, the tribological characteristics are yet to be fully understood. With a view to incorporation in microelectromechanical and nanoelectromechanical systems (MEMS and NEMS, respectively), BNNS has been studied both as a solid and as a liquid lubricant additive. As a solid lubricant on top of Cu substrate, h-BN in mostly monolayer form is found to reduce the friction of the Cu substrate by a factor of 40 [258]. Dispersion of mono- to few-layer BNNS in water was found to reduce the friction and wear of SiC ball bearings sliding on a silicon wafer [259]. The formation of tribofilms containing BNNS on the wear tracks was believed to improve the tribological performance of the dispersion [259].

In-depth AFM studies on mono- to few-layer 2D materials (graphene, h-BN, MoS_2, $NbSe_2$) have revealed an increase in friction at the tip-nanosheet interface when the layer number decreases [215]. The low bending stiffness of the 2D material compared to its in-plane stiffness can cause the sheet to pucker when the tip approaches the sheet. These out-of-plane puckered regions act as a barrier against tip sliding, contributing to increased friction for 2D materials with reduced layer numbers [215].

6.6. Air stability of BNNS

Similar to its bulk form, few-layered h-BN has been found to be stable in air at elevated temperatures (up to 850°C) [260]. Oxidation of monolayer h-BN, however, starts at 700 °C [260]. At 850 ºC, monolayer h-BN is highly oxidized and randomly oriented etching lines in the sheet are generated (Figure 12a). BNNS has been used to protect metal surfaces at elevated temperatures. A BNNS coating, about 5 nm thick, was found to protect Ni and stainless steel up to 1100 °C, and up to 500 °C in the case of Cu substrate (Figure 12b, c) in a 300 mTorr oxygen atmosphere for 30 minutes [123]. BNNS has been employed as a fire resistant coating for wood, which does not carbonize up to 900 °C [261]. Epoxy based composite incorporating air-exfoliated BNNS has also shown good flame retardant properties [262].
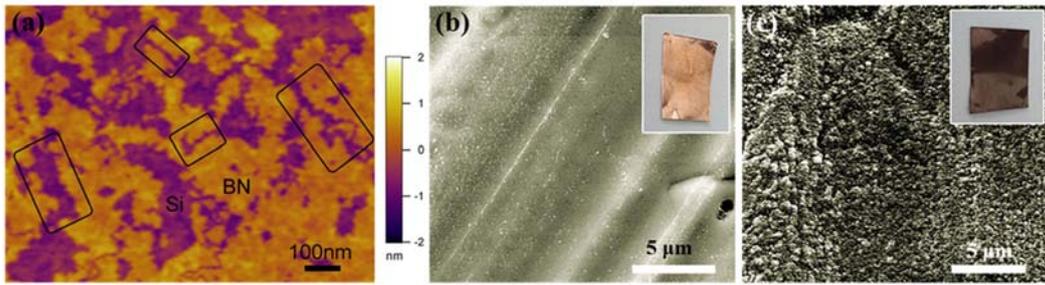
Figure 12: BNNS protection of substrates against oxidation. (a) AFM image of monolayer BNNS on Si wafer treated at 850 °C in air. The etched lines are highlighted in the boxes. Reproduced with permission from ref. 253. Copyright 2014 American Chemical Society. SEM image of Cu substrate (b) with and (c) without BNNS coating after oxidation at 1100 °C in a 300 mTorr oxygen environment for 30 minutes. Insets in each image are optical images of the samples after oxidation. Adapted with permission from ref. 123. Copyright 2013 Nature Publishing Group.

7. Conclusions

BNNS has been studied as a key component, mainly for substrates, in 2D nanoscale electronics. BNNS has also shown great potential as an atomically-thin protection layer. All these applications necessitate BNNS that has a large lateral size, is free of defects, and has a desirable thickness. The CVD method is arguably the best method to produce BNNS with these characteristics. In this review, we have summarized the recent advances in the CVD growth of BNNS, its characterization techniques, and the various applications utilizing its unique properties.

The properties of two key parameters for the CVD process, the precursors and substrates, have been enumerated, and their impacts on the quality of BNNS have been discussed in terms of thickness, lateral sizes, and homogeneity. There are two types of precursors: single molecules containing both B and N atoms, and multiple sources that contain B and N separately. These precursors have been employed in different CVD systems, such as UHV-CVD, AP-CVD, and LP-CVD. Treatments of the substrate prior to growth, including thermal annealing, electropolishing, and melting, have proved critical for growing large crystalline BNNS. In particular, BNNS grown on melted Cu is particularly large and predominantly 1-2 atomic layers in thickness. The exact growth mechanism is still unclear and deserves investigation. Similarly, growth can be attempted on other melted liquid surfaces, which may lead to even larger BNNS with better control over thickness.

35

More efforts should be devoted to understanding the origin of *h*-BN stacking orders. Growing BNNS on different substrates such as Ni and Pt, and comparing the stacking order with that grown on Cu may help to explain the impact of substrates. It would also be highly valuable to investigate the correlation between stacking orders and physical properties.

The characterisation of BNNS needs some special knowledge and tools in order to obtain the most reliable results. We have thus presented a comprehensive review on the microscopies and spectroscopies used to investigate BNNS, highlighting the advantages and disadvantages of the various techniques.

Being atomically flat, highly insulating, impermeable to small molecules, having high in-plane thermal conductivity, and high thermal and chemical stability, BNNS has been confirmed to be ideal for many applications, including substrates in 2D nanoelectronics, means of ultra-thin passivation, and fillers to improve mechanical properties and/or to enhance thermal conductivity of polymers. As the family of 2D materials is constantly expanding, BNNS may be used as a good substrate for new hybrid devices.

8. Acknowledgements

Notes and references

[1]   H.W. Kroto, J.R. Heath, S.C. O'Brien, R.F. Curl, R.E. Smalley, Nature 318 (1985) 162–163.

[2]   S. Iijima, Nature 354 (1991) 56–58.

[3]   H.P. Boehm, A. Clauss, G.O. Fischer, U. Hofmann, Zeitschrift Für Anorg. Und Allg. Chemie 316 (1962) 119–127.

[4]   A. Nagashima, N. Tejima, Y. Gamou, T. Kawai, C. Oshima, Phys. Rev. Lett. 75 (1995) 3918–3921.

[5]   A. Nagashima, N. Tejima, Y. Gamou, T. Kawai, C. Oshima, Phys. Rev. B 51 (1995) 4606–4613.

[6]   K.S. Novoselov, Science 306 (2004) 666–669.

[7]   S. V. Morozov, K.S. Novoselov, M.I. Katsnelson, F. Schedin, D.C. Elias, J.A. Jaszczak, A.K. Geim, Phys. Rev. Lett. 100 (2008) 16602.

[8]   K.S. Novoselov, D. Jiang, F. Schedin, T.J. Booth, V. V Khotkevich, S. V Morozov, A.K. Geim, Proc. Natl. Acad. Sci. U. S. A. 102 (2005) 10451–3.

[9]   J.N. Coleman, M. Lotya, A. O'Neill, S.D. Bergin, P.J. King, U. Khan, K. Young, A. Gaucher, S. De, R.J. Smith, I. V Shvets, S.K. Arora, G. Stanton, H.-Y. Kim, K. Lee, G.T. Kim, G.S. Duesberg, T. Hallam, J.J. Boland, J.J. Wang, J.F. Donegan, J.C. Grunlan, G. Moriarty, A. Shmeliov, R.J. Nicholls, J.M. Perkins, E.M. Grieveson, K. Theuwissen, D.W. McComb, P.D. Nellist, V. Nicolosi, Science 331 (2011) 568–71.

[10]   B. Aufray, A. Kara, S. Vizzini, H. Oughaddou, C. Léandri, B. Ealet, G. Le Lay, Appl. Phys. Lett. 96 (2010) 183102.

[11]   H. Liu, A.T. Neal, Z. Zhu, Z. Luo, X. Xu, D. Tománek, P.D. Ye, ACS Nano 8 (2014) 4033–4041.

[12]   L. Li, Y. Yu, G.J. Ye, Q. Ge, X. Ou, H. Wu, D. Feng, X.H. Chen, Y. Zhang, Nat. Nanotech. 9 (2014) 372–377.

[13]   M.E. Dávila, L. Xian, S. Cahangirov, A. Rubio, G. Le Lay, New J. Phys. 16 (2014) 95002.

[14]   E. Gibney, Nature 522 (2015) 8–10.

[15]   D. Akinwande, N. Petrone, J. Hone, Nat. Commun. 5 (2014) 5678.

[16]   C.R. Dean, A.F. Young, I. Meric, C. Lee, L. Wang, S. Sorgenfrei, K. Watanabe, T. Taniguchi, P. Kim, K.L. Shepard, J. Hone, Nat. Nanotech. 5 (2010) 722–6.

[17]   R.T. Weitz, A. Yacoby, Nat. Nanotech. 5 (2010) 699–700.

[18]   M.S. Bresnehan, M.J. Hollander, M. Wetherington, M. LaBella, K.A. Trumbull, R. Cavalero, D.W. Snyder, J.A. Robinson, ACS Nano 6 (2012) 5234–5241.

[19]   K.K. Kim, A. Hsu, X. Jia, S.M. Kim, Y. Shi, M. Dresselhaus, T. Palacios, J Kong, ACS Nano 6 (2012) 8583–8590.

[20]   K.H. Lee, H.-J. Shin, J. Lee, I. Lee, G.-H. Kim, J.-Y. Choi, S.-W. Kim, Nano Lett. 12 (2012) 714–718.

[21]   L. Wang, B. Wu, J. Chen, H. Liu, P. Hu, Y. Liu, Adv. Mater. 26 (2014) 1559–1564.

[22]   G.-H. Lee, Y. Yu, X. Cui, N. Petrone, C.-H. Lee, M.S. Choi, D.-Y. Lee, C. Lee, W.J. Yoo, K. Watanabe, T. Taniguchi, C. Nuckolls, P. Kim, J. Hone, ACS Nano 7 (2013) 7931–7936.

[23]   A. Pakdel, Y. Bando, D. Golberg, Chem. Soc. Rev. 43 (2014) 934–959.

[24]   H. Pedersen, M. Chubarov, H. Högberg, J. Jensen, A. Henry, Thin Solid Films 520 (2012) 5889–5893.

[25]   Z. Zhao, Z. Yang, Y. Wen, Y. Wang, J. Am. Ceram. Soc. 94 (2011) 4496–4501.

[26]   S. Alkoy, C. Toy, T. Gönül, A. Tekin, J. Eur. Ceram. Soc. 2219 (1997) 1415–1422.

[27]   N.G. Chopra, R.J. Luyken, K. Cherrey, V.H. Crespi, M.L. Cohen, S.G. Louie, A. Zettl, Science 269 (1995) 966–967.

[28]   D. Golberg, Y. Bando, O. Stéphan, K. Kurashima, Appl. Phys. Lett. 73 (1998) 2441.

[29]   M. Terrones, J.-C. Charlier, A. Gloter, E. Cruz-Silva, E. Terrés, Y.B. Li, A. Vinu, Z. Zanolli, J.M. Dominguez, H. Terrones, Y. Bando, D. Golberg, Nano Lett. 8 (2008) 1026–32.

[30]   Z.-G. Chen, J. Zou, G. Liu, F. Li, Y. Wang, L. Wang, X.-L. Yuan, T. Sekiguchi, H.-M. Cheng, G.Q. Lu, ACS Nano 2 (2008) 2183–2191.

[31]   G.M. Ingo, G. Padeletti, T. de Caro, C. Riccucci, F. Faraldi, A. Curulli, A. Mezzi, M. Piccinini, J. Mater. Chem. 21 (2011) 10268.

[32]   F.L. Deepak, C.P. Vinod, K. Mukhopadhyay, A. Govindaraj, C.N.R. Rao, Chem. Phys. Lett. 353 (2002) 345–352.

[33]   Y. Qiu, J. Yu, J. Yin, C. Tan, X. Zhou, X. Bai, E. Wang, Nanotechnology 20 (2009) 345603.

[34]   M. Zheng, Y. Gu, Z. Xu, Y. Liu, Mater. Lett. 61 (2007) 1943–1945.

[35]   Y. Yu, H. Chen, Y. Liu, T. White, Y. Chen, Mater. Lett. 80 (2012) 148–151.

[36]   A. Pakdel, Y. Bando, D. Golberg, Langmuir 29 (2013) 7529–7533.

[37]   Q. Weng, X. Wang, C. Zhi, Y. Bando, D. Golberg, ACS Nano 7 (2013) 1558–1565.

[38]   J. Yin, X. Li, J. Zhou, W. Guo, Nano Lett. 13 (2013) 3232–3236.

[39]   Y. Liu, S. Bhowmick, B.I. Yakobson, Nano Lett. 11 (2011) 3113–3116.

[40]   W. Auwa, H.U. Suter, H. Sachdev, T. Greber, Chem. Mater. 16 (2004) 343–345.

[41]   R. Mukherjee, S. Bhowmick, J. Chem. Theory Comput. 7 (2011) 720–724.

[42]   B. Huang, H. Lee, B.-L. Gu, F. Liu, W. Duan, Nano Res. 5 (2011) 62–72.

[43]   Z. Zhang, Y. Liu, Y. Yang, B.I. Yakobson, Nano Lett. 16 (2016) 1398–1403.

[44]   R.Y. Tay, M.H. Griep, G. Mallick, S.H. Tsang, R.S. Singh, T. Tumlin, E.H.T. Teo, S.P. Karna, Nano Lett. 14 (2014) 839–846.

[45]   C.-J. Kim, L. Brown, M.W. Graham, R. Hovden, R.W. Havener, P.L. McEuen, D.A. Muller, J. Park, Nano Lett. 13 (2013) 5660–5665.

[46]   R.M. Ribeiro, N.M.R. Peres, Phys. Rev. B 83 (2011) 235312.

[47]   G. Constantinescu, A. Kuc, T. Heine, Phys. Rev. Lett. 111 (2013) 36104.

[48]   A. Shmeliov, J.S. Kim, K.B. Borisenko, P. Wang, E. Okunishi, M. Shannon, A.I. Kirkland, P.D. Nellist,

V. Nicolosi, Nanoscale 5 (2013) 2290–2294.

[49]   M.H. Khan, G. Casillas, D.R.G. Mitchell, H.K. Liu, L. Jiang, Z. Huang, Nanoscale 8 (2016) 15926–15933.

[50]   N. Marom, J. Bernstein, J. Garel, A. Tkatchenko, E. Joselevich, L. Kronik, O. Hod, Phys. Rev. Lett. 105 (2010) 46801.

[51]   X. Li, L. Basile, M. Yoon, C. Ma, A.A. Puretzky, J. Lee, J.C. Idrobo, M. Chi, C.M. Rouleau, D.B. Geohegan, K. Xiao, Angew. Chemie Int. Ed. 54 (2015) 2712–2717.

[52]   M. Xia, B. Li, K. Yin, G. Capellini, G. Niu, Y. Gong, W. Zhou, P.M. Ajayan, Y.-H. Xie, ACS Nano 9 (2015) 12246–12254.

[53]   J.-U. Lee, K. Kim, S. Han, G.H. Ryu, Z. Lee, H. Cheong, ACS Nano 10 (2016) 1948–1953.

[54]   Q. Li, X. Zou, M. Liu, J. Sun, Y. Gao, Y. Qi, X. Zhou, B.I. Yakobson, Y. Zhang, Z. Liu, Nano Lett. 15 (2015) 5804–5810.

[55]   A.L. Gibb, N. Alem, J.-H. Chen, K.J. Erickson, J. Ciston, A. Gautam, M. Linck, A. Zettl, J. Am. Chem. Soc. 135 (2013) 6758–6761.

[56]   L. Song, L. Ci, H. Lu, P.B. Sorokin, C. Jin, J. Ni, A.G. Kvashnin, D.G. Kvashnin, J. Lou, B.I. Yakobson, P.M. Ajayan, Nano Lett. 10 (2010) 3209–3215.

[57]   H. Nozaki, S. Itoh, J. Phys. Chem. Solids 57 (1996) 41–49.

[58]   V. V Pokropivny, V. V Skorokhod, G.S. Oleinik, A. V Kurdyumov, T.S. Bartnitskaya, A. V Pokropivny, A.G. Sisonyuk, D.M. Sheichenko, J. Solid State Chem. 154 (2000) 214–222.

[59]   Y. Liu, X. Zou, B.I. Yakobson, ACS Nano 6 (2012) 7053–7058.

[60]   O. Cretu, Y. Lin, K. Suenaga, Nano Lett. 14 (2014) 1064–1068.

[61]   A. Lyalin, A. Nakayama, K. Uosaki, T. Taketsugu, Phys. Chem. Chem. Phys. 15 (2013) 2809–20.

[62]   C. Jin, F. Lin, K. Suenaga, S. Iijima, Phys. Rev. Lett. 102 (2009) 195505.

[63]   J. Meyer, A. Chuvilin, G. Algara-Siller, Nano Lett. 9 (2009) 2683–2689.

[64]   N. Alem, R. Erni, C. Kisielowski, M.D. Rossell, W. Gannett, A. Zettl, Phys. Rev. B 80 (2009) 155425.

[65]   M.H. Khan, Z. Huang, F. Xiao, G. Casillas, Z. Chen, P.J. Molino, H.K. Liu, Sci. Rep. 5 (2015) 7743.

[66]   W.H. Balmain, J. Prakt. Chem. 27 (1842) 422–430.

[67]   S. Rudolph, Am. Ceram. Soc. Bull. 79 (2000) 50.

[68]   A. Lipp, K.A. Schwetz, K. Hunold, J. Eur. Ceram. Soc. 5 (1989) 3–9.

[69]   L. Wang, I. Meric, P. Huang, Q. Gao, Y. Gao, Science 342 (2013) 614–617.

[70]   N. Petrone, T. Chari, I. Meric, L. Wang, K.L. Shepard, J. Hone, ACS Nano 9 (2015) 8953–8959.

[71]   G. Zhao, F. Zhang, Y. Wu, X. Hao, Z. Wang, X. Xu, Adv. Opt. Mater. 4 (2016) 141–146.

[72]   Z. Zeng, T. Sun, J. Zhu, X. Huang, Z. Yin, G. Lu, Z. Fan, Q. Yan, H.H. Hng, H. Zhang, Angew. Chemie Int. Ed. 51 (2012) 9052–9056.

[73]   N.I. Kovtyukhova, Y. Wang, R. Lv, M. Terrones, V.H. Crespi, T.E. Mallouk, J. Am. Chem. Soc. 135 (2013) 8372–8381.

[74]   M. Du, Y. Wu, X. Hao, CrystEngComm 15 (2013) 1782.

[75]   Y. Lin, T. V. Williams, J.W. Connell, J. Phys. Chem. Lett. 1 (2010) 277–283.

[76]   M.J. Rand, J.F. Roberts, J. Electrochem. Soc. 115 (1968) 423–429.

[77]   H. Pierson, in:, Handb. Chem. Vap. Depos., 2nd ed., Noyes Publications, New York, 1999.

[78]   T. Takahashi, H. Itoh, A. Takeuchi, J. Cryst. Growth 47 (1979) 245–250.

[79]   M. Sano, M. Aoki, Thin Solid Films 83 (1981) 247–251.

[80]   S. Arya, A. D'amico, Thin Solid Films 157 (1988) 267–282.

[81]   R. Paine, C. Narula, Chem. Rev. 90 (1990) 73–91.

[82]   A.R. Phani, Bull. Mater. Sci. 17 (1994) 219–224.

[83]   J. Li, S. Bernard, V. Salles, C. Gervais, P. Miele, D. Lyon, D. France, M. Berthelot, Chem. Mater. 22 (2010) 2920–2929.

[84]   F. Müller, K. Stöwe, H. Sachdev, Chem. Mater. 17 (2005) 3464–3467.

[85]   Y. Stehle, H.M. Meyer, R.R. Unocic, M. Kidder, G. Polizos, P.G. Datskos, R. Jackson, S.N. Smirnov, I. V. Vlassiouk, Chem. Mater. 27 (2015) 8041–8047.

[86]   K.K. Kim, A. Hsu, X. Jia, S.M. Kim, Y. Shi, M. Hofmann, D. Nezich, J.F. Rodriguez-Nieva, M. Dresselhaus, T. Palacios, J. Kong, Nano Lett. 12 (2012) 161–166.

[87]   G. Lu, T. Wu, Q. Yuan, H. Wang, H. Wang, F. Ding, X. Xie, M. Jiang, Nat. Commun. 6 (2015) 6160.

[88]   Y. Gao, W. Ren, T. Ma, Z. Liu, Y. Zhang, W.-B. Liu, L.-P. Ma, X. Ma, H.-M. Cheng, ACS Nano 7 (2013) 5199–5206.

[89]   S. Frueh, R. Kellett, C. Mallery, T. Molter, W.S. Willis, C. King'ondu, S.L. Suib, Inorg. Chem. 50 (2011) 783–792.

[90]   G.R. Whittell, I. Manners, Angew. Chemie Int. Ed. 50 (2011) 10288–10289.

[91]   M. Son, H. Lim, M. Hong, H.C. Choi, Nanoscale 3 (2011) 3089–3093.

[92]   G. Kim, A.-R. Jang, H.Y. Jeong, Z. Lee, D.J. Kang, H.S. Shin, Nano Lett. 13 (2013) 1834–1839.

[93]   L. Qin, J. Yu, M. Li, F. Liu, X. Bai, Nanotechnology 22 (2011) 215602.

[94]   J. Yu, L. Qin, Y. Hao, S. Kuang, X. Bai, Y.-M. Chong, W. Zhang, E. Wang, ACS Nano 4 (2010) 414–
        422.

[95]   L. Qin, J. Yu, S. Kuang, C. Xiao, X. Bai, Nanoscale 4 (2012) 120–123.

[96]   C. Zhang, X. Hao, Y. Wu, M. Du, Mater. Res. Bull. 47 (2012) 2277–2281.

[97]   A. Ismach, H. Chou, D.A. Ferrer, Y. Wu, S. McDonnell, H.C. Floresca, A. Covacevich, C. Pope, R.
        Piner, M.J. Kim, R.M. Wallace, L. Colombo, R.S. Ruoff, ACS Nano 6 (2012) 6378–85.

[98]   D. Ammonia, S. Chatterjee, Z. Luo, M. Acerce, D.M. Yates, A.T.C. Johnson, L.G. Sneddon, Chem.
        Mater. 23 (2011) 4414–4416.

[99]   F. Müller, S. Hüfner, H. Sachdev, S. Gsell, M. Schreck, Phys. Rev. B 82 (2010) 75405.

[100]   N. Guo, J. Wei, L. Fan, Y. Jia, D. Liang, H. Zhu, K. Wang, D. Wu, Nanotechnology 23 (2012) 415605.

[101]   X. Wang, A. Pakdel, C. Zhi, K. Watanabe, T. Sekiguchi, D. Golberg, Y. Bando, J. Phys. Condens. Matter
        24 (2012) 314205.

[102]   J. Han, J.-Y. Lee, H. Kwon, J.-S. Yeo, Nanotechnology 25 (2014) 145604.

[103]   A.-R. Jang, S. Hong, C. Hyun, S.I. Yoon, G. Kim, H.Y. Jeong, T.J. Shin, S.O. Park, K. Wong, S.K.
        Kwak, N. Park, K. Yu, E. Choi, A. Mishchenko, F. Withers, K.S. Novoselov, H. Lim, H.S. Shin, Nano
        Lett. 16 (2016) 3360–3366.

[104]   C. Rohr, J. Boo, W. Ho, Thin Solid Films 322 (1998) 9–13.

[105]   S.M. Kim, A. Hsu, P.T. Araujo, Y.-H. Lee, T. Palacios, M. Dresselhaus, J.-C. Idrobo, K.K. Kim, J. Kong,
        Nano Lett. 13 (2013) 933–41.

[106]   Z. Liu, L. Song, S. Zhao, J. Huang, L. Ma, J. Zhang, J. Lou, P.M. Ajayan, Nano Lett. 11 (2011) 2032–
        2037.

[107]   Z. Liu, L. Ma, G. Shi, W. Zhou, Y. Gong, S. Lei, X. Yang, J. Zhang, J. Yu, K.P. Hackenberg, A.
        Babakhani, J.-C. Idrobo, R. Vajtai, J. Lou, P.M. Ajayan, Nat. Nanotech. 8 (2013) 119–24.

[108]   S. Behura, P. Nguyen, S. Che, R. Debbarma, V. Berry, J. Am. Chem. Soc. 137 (2015) 13060–13065.

[109]   R. Tay, S. Tsang, M. Loeblein, Appl. Phys. Lett. 106 (2015) 1–6.

[110]   X. Yang, Z. Guan, M. Zeng, J. Wei, W. Wang, X. Bai, Small 9 (2013) 1353–1358.

[111] M.S. Bresnehan, M.J. Hollander, M. Wetherington, K. Wang, T. Miyagi, G. Pastir, D.W. Snyder, J.J. Gengler, A. a. Voevodin, W.C. Mitchel, J. a. Robinson, J. Mater. Res. 29 (2013) 459–471.

[112] L. Wang, B. Wu, L. Jiang, J. Chen, Y. Li, Adv. Mater. 2015001166 (2015) 1–7.

[113] S. Sharma, G. Kalita, R. Vishwakarma, Sci. Rep. 5 (2015) 10426.

[114] J.-H. Park, J.C. Park, S.J. Yun, H. Kim, D.H. Luong, S.M. Kim, S.H. Choi, W. Yang, J. Kong, K.K. Kim, Y.H. Lee, ACS Nano 8 (2014) 8520–8528.

[115] J. Yin, X. Liu, W. Lu, J. Li, Y. Cao, Y. Li, Y. Xu, X. Li, J. Zhou, C. Jin, W. Guo, Small 11 (2015) 5375–5380.

[116] C.M. Orofeo, S. Suzuki, H. Kageshima, H. Hibino, Nano Res. 6 (2013) 335–347.

[117] R.Y. Tay, H.J. Park, G.H. Ryu, D. Tan, S.H. Tsang, H. Li, W. Liu, E.H.T. Teo, Z. Lee, Y. Lifshitz, R.S. Ruoff, Nanoscale 8 (2016) 2434–2444.

[118] A. Pakdel, X. Wang, C. Zhi, Y. Bando, K. Watanabe, T. Sekiguchi, T. Nakayama, D. Golberg, J. Mater. Chem. 22 (2012) 4818.

[119] P. Sutter, J. Lahiri, P. Albrecht, E. Sutter, ACS Nano 5 (2011) 7303–7309.

[120] Y.-H. Lee, K.-K. Liu, A.-Y. Lu, C.-Y. Wu, C.-T. Lin, W. Zhang, C.-Y. Su, C.-L. Hsu, T.-W. Lin, K.-H. Wei, Y. Shi, L.-J. Li, RSC Adv. 2 (2012) 111–115.

[121] J. Lu, P.S.E. Yeo, Y. Zheng, H. Xu, C.K. Gan, M.B. Sullivan, A.H. Castro Neto, K.P. Loh, J. Am. Chem. Soc. 135 (2013) 2368–73.

[122] M.S. Bresnehan, G.R. Bhimanapati, K. Wang, D.W. Snyder, J.A. Robinson, ACS Appl. Mater. Interfaces 6 (2014) 16755–16762.

[123] Z. Liu, Y. Gong, W. Zhou, L. Ma, J. Yu, J.C. Idrobo, J. Jung, A.H. MacDonald, R. Vajtai, J. Lou, P.M. Ajayan, Nat. Commun. 4 (2013) 1–8.

[124] H. Oh, J. Jo, Y. Tchoe, H. Yoon, H. Hwi Lee, S.-S. Kim, M. Kim, B.-H. Sohn, G.-C. Yi, NPG Asia Mater. 8 (2016) e330.

[125] S. Caneva, R.S. Weatherup, B.C. Bayer, B. Brennan, S.J. Spencer, K. Mingard, A. Cabrero-Vilatela, C. Baehtz, A.J. Pollard, S. Hofmann, Nano Lett. 15 (2015) 1867–1875.

[126] S. Caneva, R.S. Weatherup, B.C. Bayer, R. Blume, A. Cabrero-Vilatela, P. Braeuninger-Weimer, M.-B. Martin, R. Wang, C. Baehtz, R. Schloegl, J.C. Meyer, S. Hofmann, Nano Lett. 16 (2016) 1250–1261.

[127] M. Corso, Science 303 (2004) 217–220.

[128] Y. Shi, C. Hamsen, X. Jia, K.K. Kim, A. Reina, M. Hofmann, A.L. Hsu, K. Zhang, H. Li, Z.-Y. Juang, M.S. Dresselhaus, L.-J. Li, J. Kong, Nano Lett. 10 (2010) 4134–4139.

[129] N.A. Vinogradov, A.A. Zakharov, M.L. Ng, A. Mikkelsen, E. Lundgren, A.B. Preobrajenski, Langmuir 28 (2012) 1775–1781.

[130] F. Orlando, R. Larciprete, J. Phys. Chem. C 116 (2011) 157–164.

[131] P. Kidambi, R. Blume, J. Kling, Chem. Mater. 26 (2014) 6380–6392.

[132] F. Müller, S. Hüfner, H. Sachdev, R. Laskowski, P. Blaha, K. Schwarz, Phys. Rev. B 82 (2010) 113406.

[133] M. Wang, M. Kim, D. Odkhuu, N. Park, J. Lee, W.-J. Jang, S.-J. Kahng, R.S. Ruoff, Y.J. Song, S. Lee, ACS Nano 8 (2014) 8711.

[134] C. Gomez-Aleixandre, D. Diaz, F. Orgaz, J.M. Albella, J. Phys. Chem. 97 (1993) 11043–11046.

[135] X. Wang, T.N. Hooper, A. Kumar, I.K. Priest, Y. Sheng, T.O.M. Samuels, S. Wang, A.W. Robertson, M. Pacios, H. Bhaskaran, A.S. Weller, J.H. Warner, CrystEngComm 19 (2017) 285–294.

[136] R.Y. Tay, H. Li, S.H. Tsang, M. Zhu, M. Loeblein, L. Jing, F.N. Leong, E.H.T. Teo, Chem. Mater. 28 (2016) 2180–2190.

[137] A.B. Preobrajenski, A.S. Vinogradov, N. Mårtensson, Surf. Sci. 582 (2005) 21–30.

[138] R. Laskowski, P. Blaha, K. Schwarz, Phys. Rev. B 78 (2008) 45409.

[139] M. Bokdam, G. Brocks, M.I. Katsnelson, P.J. Kelly, Phys. Rev. B 90 (2014) 85415.

[140] F. Müller, S. Hüfner, H. Sachdev, Surf. Sci. 602 (2008) 3467–3476.

[141] S.M. Kim, A. Hsu, M.H. Park, S.H. Chae, S.J. Yun, J.S. Lee, D.-H. Cho, W. Fang, C. Lee, T. Palacios, M. Dresselhaus, K.K. Kim, Y.H. Lee, J. Kong, Nat. Commun. 6 (2015) 8662.

[142] P.C. Yang, J.T. Prater, W. Liu, J.T. Glass, R.F. Davis, J. Electron. Mater. 34 (2005) 1558–1564.

[143] P. Sutter, J. Lahiri, P. Zahl, B. Wang, E. Sutter, Nano Lett. 13 (2013) 276–281.

[144] M. Morscher, M. Corso, T. Greber, J. Osterwalder, Surf. Sci. 600 (2006) 3280–3284.

[145] L. Camilli, E. Sutter, P. Sutter, 2D Mater. 1 (2014) 25003.

[146] G. Grad, P. Blaha, K. Schwarz, W. Auwärter, T. Greber, Phys. Rev. B 68 (2003) 1–7.

[147] J.K. Hite, Z.R. Robinson, C.R. Eddy, B.N. Feigelson, ACS Appl. Mater. Interfaces 7 (2015) 15200–15205.

[148] Q. Wu, J.-H. Park, S. Park, S.J. Jung, H. Suh, N. Park, W. Wongwiriyapan, S. Lee, Y.H. Lee, Y.J. Song, Sci. Rep. 5 (2015) 16159.

[149] H. Cho, S. Park, D.-I. Won, S.O. Kang, S.-S. Pyo, D.-I. Kim, S.M. Kim, H.C. Kim, M.J. Kim, Sci. Rep. 5 (2015) 11985.

[150] J. Dias, P.R. Kidambi, S. Hofmann, C. Ducati, J. Phys. Conf. Ser. 522 (2014) 12070.

[151] C.-K. Chang, S. Kataria, C.-C. Kuo, A. Ganguly, B.-Y. Wang, J.-Y. Hwang, K.-J. Huang, W.-H. Yang, S.-B. Wang, C.-H. Chuang, M. Chen, C.-I. Huang, W.-F. Pong, K.-J. Song, S.-J. Chang, J.-H. Guo, Y. Tai, M. Tsujimoto, S. Isoda, C.-W. Chen, L.-C. Chen, K.-H. Chen, ACS Nano 7 (2013) 1333–1341.

[152] W. Wu, L.A. Jauregui, Z. Su, Z. Liu, J. Bao, Y.P. Chen, Q. Yu, Adv. Mater. 23 (2011) 4898–4903.

[153] A.M. Lewis, B. Derby, I.A. Kinloch, ACS Nano 7 (2013) 3104–3117.

[154] Z. Yan, J. Lin, Z. Peng, Z. Sun, Y. Zhu, L. Li, C. Xiang, E.L. Samuel, C. Kittrell, J.M. Tour, ACS Nano 6 (2012) 9110–9117.

[155] R.S. Edwards, K.S. Coleman, Acc. Chem. Res. 46 (2013) 23–30.

[156] A.E. Paths, G. Nucleation, ACS Nano 6 (2012) 3614–3623.

[157] Z. Yan, J. Lin, Z. Peng, Z. Sun, Y. Zhu, L. Li, C. Xiang, E.L. Samuel, C. Kittrell, J.M. Tour, ACS Nano 6 (2012) 9110–9117.

[158] M.T. Paffett, R.J. Simonson, P. Papin, R.T. Paine, Surf. Sci. 232 (1990) 286–296.

[159] H.O. T.B. Massalski, Binary Alloy Phase Diagrams, 2nd ed., ASM International: Materials Park, Ohio, 1990.

[160] M. Okada, T. Sawazaki, K. Watanabe, T. Taniguch, H. Hibino, H. Shinohara, R. Kitaura, ACS Nano 8 (2014) 8273–8277.

[161] J.A. Venables, Introduction to Surface and Thin Film Processes, Cambridge University Press, New York, 2000.

[162] X. Li, W. Cai, J. An, S. Kim, J. Nah, D. Yang, R. Piner, A. Velamakanni, I. Jung, E. Tutuc, S.K. Banerjee, L. Colombo, R.S. Ruoff, Science 324 (2009) 1312–1314.

[163] J.W. Suk, A. Kitt, C.W. Magnuson, Y. Hao, S. Ahmed, J. An, A.K. Swan, B.B. Goldberg, R.S. Ruoff, ACS Nano 5 (2011) 6916–6924.

[164] J. Kang, D. Shin, S. Bae, B.H. Hong, Nanoscale 4 (2012) 5527–5537.

[165] W. Regan, N. Alem, B. Alemán, B. Geng, Appl. Phys. Lett. 96 (2010) 10–13.

[166] Y. Lee, S. Bae, H. Jang, S. Jang, S. Zhu, S.H. Sim, Y. Il Song, B.H. Hong, J. Ahn, Nano Lett. 10 (2010) 490–493.

44

[167] S. Bae, H. Kim, Y. Lee, X. Xu, J. Park, Y. Zheng, J. Balakrishnan, T. Lei, H. Ri Kim, Y. Il Song, Y.-J. Kim, K.S. Kim, B. Özyilmaz, J.-H. Ahn, B.H. Hong, S. Iijima, Nat. Nanotech. 5 (2010) 574–578.

[168] D.-Y. Wang, I.-S. Huang, P.-H. Ho, S.-S. Li, Y.-C. Yeh, D.-W. Wang, W.-L. Chen, Y.-Y. Lee, Y.-M. Chang, C.-C. Chen, C.-T. Liang, C.-W. Chen, Adv. Mater. 25 (2013) 4521–4526.

[169] F. Amet, J.R. Williams, A.G.F. Garcia, M. Yankowitz, K. Watanabe, T. Taniguchi, D. Goldhaber-Gordon, Phys. Rev. B 85 (2012) 73405.

[170] Y. Song, C. Zhang, B. Li, D. Jiang, G. Ding, H. Wang, X. Xie, Appl. Surf. Sci. 313 (2014) 647–653.

[171] R. Sevak Singh, R. Yingjie Tay, W. Leong Chow, S. Hon Tsang, G. Mallick, E.H. Tong Teo, Appl. Phys. Lett. 104 (2014) 163101.

[172] M. Wang, S.K. Jang, W.-J. Jang, M. Kim, S.-Y. Park, S.-W. Kim, S.-J. Kahng, J.-Y. Choi, R.S. Ruoff, Y.J. Song, S. Lee, Adv. Mater. 25 (2013) 2746–2752.

[173] A.G.F. Garcia, M. Neumann, F. Amet, J.R. Williams, K. Watanabe, T. Taniguchi, D. Goldhaber-Gordon, Nano Lett. 13 (2013) 2314–2314.

[174] P.Y. Huang, C.S. Ruiz-Vargas, A.M. van der Zande, W.S. Whitney, M.P. Levendorf, J.W. Kevek, S. Garg, J.S. Alden, C.J. Hustedt, Y. Zhu, J. Park, P.L. McEuen, D.A. Muller, Nature 469 (2011) 389–392.

[175] A. Gibb, N. Alem, A. Zettl, Phys. Status Solidi (B) 250 (2013) 2727–2731.

[176] D.M. Mattox, Handbook of Physical Vapor Deposition (PVD) Processing, 2nd ed., William Andrew, 2010.

[177] H. Wang, X. Zhang, H. Liu, Z. Yin, J. Meng, J. Xia, X.M. Meng, J. Wu, J. You, Adv. Mater. 27 (2015) 8109–8115.

[178] H. Wang, X. Zhang, J. Meng, Z. Yin, X. Liu, Y. Zhao, L. Zhang, Small 11 (2015) 1542–1547.

[179] J.H. Meng, X.W. Zhang, H.L. Wang, X.B. Ren, C.H. Jin, Z.G. Yin, X. Liu, H. Liu, Nanoscale 7 (2015) 16046–53.

[180] M. Sajjad, M. Ahmadi, M.J.-F. Guinel, Y. Lin, P. Feng, J. Mater. Sci. 48 (2012) 2543–2549.

[181] W.-Q. Han, H.-G. Yu, Z. Liu, Appl. Phys. Lett. 98 (2011) 203112.

[182] T.-W. Lin, C.-Y. Su, X.-Q. Zhang, W. Zhang, Y.-H. Lee, C.-W. Chu, H.-Y. Lin, M.-T. Chang, F.-R. Chen, L.-J. Li, Small 8 (2012) 1384–1391.

[183] Y. Gong, G. Shi, Z. Zhang, W. Zhou, J. Jung, W. Gao, L. Ma, Y. Yang, S. Yang, G. You, R. Vajtai, Q. Xu, A.H. MacDonald, B.I. Yakobson, J. Lou, Z. Liu, P.M. Ajayan, Nat. Commun. 5 (2014) 3193.

[184] W. Han, Y. Bando, K. Kurashima, T. Sato, Appl. Phys. Lett. 73 (1998) 3085–3087.

[185] X. Wang, Q. Weng, X. Wang, X. Li, J. Zhang, ACS Nano 8 (2014) 9081–9088.

[186] F. Xiao, Z. Chen, G. Casillas, C. Richardson, H. Li, Z. Huang, Chem. Commun. 52 (2016) 3911–3914.

[187] W. Lei, D. Portehault, D. Liu, S. Qin, Y. Chen, Nat. Commun. 4 (2013) 1777.

[188] F. Xiao, S. Naficy, G. Casillas, M.H. Khan, T. Katkus, L. Jiang, H. Liu, H. Li, Z. Huang, Adv. Mater. 27 (2015) 7196–7203.

[189] C. Wu, A.M. Soomro, F. Sun, H. Wang, Y. Huang, J. Wu, C. Liu, X. Yang, N. Gao, X. Chen, J. Kang, D. Cai, Sci. Rep. 6 (2016) 34766.

[190] R. V Gorbachev, I. Riaz, R.R. Nair, R. Jalil, L. Britnell, B.D. Belle, E.W. Hill, K.S. Novoselov, K. Watanabe, T. Taniguchi, A.K. Geim, P. Blake, Small 7 (2011) 465–468.

[191] D. Golla, K. Chattrakun, K. Watanabe, T. Taniguchi, B.J. LeRoy, A. Sandhu, Appl. Phys. Lett. 102 (2013) 161906.

[192] M. Arslan Shehzad, D. Hoang Tien, M. Waqas Iqbal, J. Eom, J.H. Park, C. Hwang, Y. Seo, Sci. Rep. 5 (2015) 13331.

[193] D.W. Kim, Y.H. Kim, H.S. Jeong, H.-T. Jung, Nat. Nanotech. 7 (2011) 29–34.

[194] J.-H. Son, S.-J. Baeck, M.-H. Park, J.-B. Lee, C.-W. Yang, J.-K. Song, W.-C. Zin, J.-H. Ahn, Nat. Commun. 5 (2014) 3484.

[195] C. Jia, J. Jiang, L. Gan, X. Guo, Sci. Rep. 2 (2012) 707.

[196] T.I. and T.S. T. Kuzuba, K. Era, Solid State Commun. 25 (1978) 863–865.

[197] D.M. Hoffman, G.L. Doll, P.C. Eklund, Phys. Rev. B 30 (1984) 6051–6056.

[198] R.J. Nemanich, S.A. Solin, R.M. Martin, Phys. Rev. B 23 (1981) 6348–6356.

[199] R. Geick, C. Perry, G. Rupprecht, Phys. Rev. 146 (1966) 543–547.

[200] Y. Lin, T. V. Williams, T.-B. Xu, W. Cao, H.E. Elsayed-Ali, J.W. Connell, J. Phys. Chem. C 115 (2011) 2679–2685.

[201] T. Sainsbury, A. Satti, P. May, Z. Wang, I. McGovern, Y.K. Gun'ko, J. Coleman, J. Am. Chem. Soc. 134 (2012) 18758–18771.

[202] G. Gao, W. Gao, E. Cannuccia, J. Taha-Tijerina, L. Balicas, A. Mathkar, T.N. Narayanan, Z. Liu, B.K. Gupta, J. Peng, Y. Yin, A. Rubio, P.M. Ajayan, Nano Lett. 12 (2012) 3518–3525.

[203] P. Sutter, E. Sutter, APL Mater. 92502 (2014) 1–7.

[204]   M.H. Khan, S.S. Jamali, A. Lyalin, P.J. Molino, L. Jiang, H.K. Liu, T. Taketsugu, Z. Huang, Adv. Mater. 29 (2017) 1603937.

[205]   G.-H. Lee, R.C. Cooper, S.J. An, S. Lee, A. van der Zande, N. Petrone, A.G. Hammerberg, C. Lee, B. Crawford, W. Oliver, J.W. Kysar, J. Hone, Science 340 (2013) 1073–1076.

[206]   A.W. Robertson, A. Bachmatiuk, Y.A. Wu, F. Schäffel, B. Büchner, M.H. Rümmeli, J.H. Warner, ACS Nano 5 (2011) 9984–9991.

[207]   P. Hartel, H. Rose, C. Dinges, Ultramicroscopy 63 (1996) 93–114.

[208]   O.L. Krivanek, M.F. Chisholm, V. Nicolosi, T.J. Pennycook, G.J. Corbin, N. Dellby, M.F. Murfitt, C.S. Own, Z.S. Szilagyi, M.P. Oxley, S.T. Pantelides, S.J. Pennycook, Nature 464 (2010) 571–574.

[209]   C.C. Ahn, Transmission Electron Energy Loss Spectrometry in Materials Science and The EELS Atlas, Wiley-VCH Verlag GmbH & Co. KGaA, Weinheim, FRG, 2004.

[210]   O. Cretu, Y.-C. Lin, M. Koshino, L.H.G. Tizei, Z. Liu, K. Suenaga, Phys. Rev. Lett. 114 (2015) 75502.

[211]   N.L. McDougall, R.J. Nicholls, J.G. Partridge, D.G. McCulloch, Microsc. Microanal. 20 (2014) 1053–1059.

[212]   P. Nemes-Incze, Z. Osváth, K. Kamarás, L.P. Biró, Carbon 46 (2008) 1435–1442.

[213]   L. Zitzler, S. Herminghaus, F. Mugele, Phys. Rev. B 66 (2002) 155436.

[214]   L.H. Li, T. Xing, Y. Chen, R. Jones, Adv. Mater. Interfaces 1 (2014) 1300132.

[215]   C. Lee, Q. Li, W. Kalb, X.-Z. Liu, H. Berger, R.W. Carpick, J. Hone, Science 328 (2010) 76–80.

[216]   Y. Xue, Q. Liu, G. He, K. Xu, L. Jiang, X. Hu, J. Hu, Nanoscale Res. Lett. 8 (2013) 49.

[217]   S. Suzuki, R.M. Pallares, H. Hibino, J. Phys. D. Appl. Phys. 45 (2012) 385304.

[218]   W. Lei, D. Portehault, R. Dimova, M. Antonietti, J. Am. Chem. Soc. 133 (2011) 7121–7127.

[219]   G.M. Ingo, G. Padeletti, Thin Solid Films 228 (1993) 276–279.

[220]   G. Westheimer, J. Opt. Soc. Am. 62 (1972) 1502–1504.

[221]   K. Watanabe, T. Taniguchi, T. Niiyama, K. Miya, M. Taniguchi, Nat. Photonics 3 (2009) 591–594.

[222]   J. Tauc, R. Grigorovici, A. Vancu, Phys. Status Solidi (B) 15 (1966) 627–637.

[223]   F. Stern, Solid State Phys. 15 (1963) 299–408.

[224]   G. Cassabois, P. Valvin, B. Gil, Nat. Photonics 10 (2016) 262–267.

[225]   Y. Zhang, X. Weng, H. Li, H. Li, M. Wei, J. Xiao, Z. Liu, M. Chen, Q. Fu, X. Bao, Nano Lett. 15 (2015) 3616–3623.

[226] A.B. Preobrajenski, S.A. Krasnikov, A.S. Vinogradov, M.L. Ng, T. Käämbre, A.A. Cafolla, N. Mårtensson, Phys. Rev. B 77 (2008) 85421.

[227] Y. Yang, Q. Fu, M. Wei, H. Bluhm, X. Bao, Nano Res. 8 (2014) 227–237.

[228] S. Joshi, D. Ecija, R. Koitz, M. Iannuzzi, A.P. Seitsonen, J. Hutter, H. Sachdev, S. Vijayaraghavan, F. Bischoff, K. Seufert, J. V. Barth, W. Auwärter, Nano Lett. 12 (2012) 5821–5828.

[229] T.T. Tran, K. Bray, M.J. Ford, M. Toth, I. Aharonovich, Nat. Nanotech. 11 (2015) 37–41.

[230] Y. Kubota, K. Watanabe, O. Tsuda, T. Taniguchi, Science 317 (2007) 932–934.

[231] A.L. Exarhos, D.A. Hopper, R.R. Grote, A. Alkauskas, L.C. Bassett, ACS Nano 11 (2017) 3328–3336.

[232] N.R. Jungwirth, B. Calderon, Y. Ji, M.G. Spencer, M.E. Flatté, G.D. Fuchs, Nano Lett. 16 (2016) 6052–6057.

[233] L. Britnell, R. V Gorbachev, R. Jalil, B.D. Belle, F. Schedin, M.I. Katsnelson, L. Eaves, S. V Morozov, A.S. Mayorov, N.M.R. Peres, A.H.C. Neto, J. Leist, A.K. Geim, L. a Ponomarenko, K.S. Novoselov, Nano Lett. 12 (2012) 1707–10.

[234] G.-H. Lee, Y. Yu, X. Cui, N. Petrone, C.-H. Lee, M.S. Choi, D.-Y. Lee, C. Lee, W.J. Yoo, K. Watanabe, T. Taniguchi, C. Nuckolls, P. Kim, J. Hone, ACS Nano 7 (2013) 7931–7936.

[235] W.S. Hummers, R.E. Offeman, J. Am. Chem. Soc. 80 (1958) 1339–1339.

[236] D.C. Marcano, D. V Kosynkin, J.M. Berlin, A. Sinitskii, Z. Sun, A. Slesarev, L.B. Alemany, W. Lu, J.M. Tour, ACS Nano 4 (2010) 4806–4814.

[237] K. Yan, H.-W. Lee, T. Gao, G. Zheng, H. Yao, H. Wang, Z. Lu, Y. Zhou, Z. Liang, Z. Liu, S. Chu, Y. Cui, Nano Lett. 14 (2014) 6016–6022.

[238] H. Cun, M. Iannuzzi, A. Hemmi, S. Roth, Nano Lett. 13 (2013) 2098–2103.

[239] L. Shen, Y. Zhao, Y. Wang, R. Song, Q. Yao, S. Chen, Y. Chai, J. Mater. Chem. A 4 (2016) 5044–5050.

[240] E. Husain, T.N. Narayanan, J.J. Taha-Tijerina, S. Vinod, R. Vajtai, P.M. Ajayan, ACS Appl. Mater. Interfaces 5 (2013) 4129–4135.

[241] J. Zhang, Y. Yang, J. Lou, Nanotechnology 27 (2016) 364004.

[242] L. Boldrin, F. Scarpa, R. Chowdhury, S. Adhikari, Nanotechnology 22 (2011) 505702.

[243] C. Lee, X. Wei, J. Kysar, J. Hone, Science 321 (2008) 385–388.

[244] C. Li, Y. Bando, C. Zhi, Y. Huang, D. Golberg, Nanotechnology 20 (2009) 385707.

[245] Z.-Q. Duan, Y.-T. Liu, X.-M. Xie, X.-Y. Ye, Chinese Chem. Lett. 24 (2013) 17–19.

[246] Y. Wang, Z. Shi, J. Yin, J. Mater. Chem. 21 (2011) 11371–11377.

[247] C.Y. Zhi, Y. Bando, C.C. Tang, H. Kuwahara, D. Golberg, Adv. Mater. 21 (2009) 2889–2890.

[248] U. Khan, P. May, A. O'Neill, A.P. Bell, E. Boussac, A. Martin, J. Semple, J.N. Coleman, Nanoscale 5 (2013) 581–587.

[249] W.-L. Song, P. Wang, L. Cao, A. Anderson, M.J. Meziani, A.J. Farr, Y.-P. Sun, Angew. Chemie Int. Ed. 51 (2012) 6498–6501.

[250] C. Sevik, A. Kinaci, J.B. Haskins, T. Çağın, Phys. Rev. B 84 (2011) 85409.

[251] T. Ouyang, Y. Chen, Y. Xie, K. Yang, Z. Bao, J. Zhong, Nanotechnology 21 (2010) 245701.

[252] A. Kumar, D. Pal, Phys. Status Solidi (B) 129 (1985) K9–K12.

[253] I. Jo, M.T. Pettes, J. Kim, K. Watanabe, T. Taniguchi, Z. Yao, L. Shi, Nano Lett. 13 (2013) 550–554.

[254] C. Zhi, Y. Xu, Y. Bando, D. Golberg, ACS Nano 5 (2011) 6571–6577.

[255] J. Taha-Tijerina, T.N. Narayanan, G. Gao, M. Rohde, D.A. Tsentalovich, M. Pasquali, P.M. Ajayan, ACS Nano 6 (2012) 1214–1220.

[256] J. Yu, X. Huang, C. Wu, X. Wu, G. Wang, P. Jiang, Polymer (Guildf). 53 (2012) 471–480.

[257] M. Engler, C. Lesniak, R. Damasch, Ceram. Forum Int. 84 (2007) 49–53.

[258] X. Li, J. Yin, J. Zhou, W. Guo, Nanotechnology 25 (2014) 105701.

[259] D.-H. Cho, J.-S. Kim, S.-H. Kwon, C. Lee, Y.-Z. Lee, Wear 302 (2013) 981–986.

[260] L.H. Li, J. Cervenka, K. Watanabe, T. Taniguchi, Y. Chen, ACS Nano 8 (2014) 1457–1462.

[261] J. Liu, R.G. Kutty, Q. Zheng, V. Eswariah, S. Sreejith, Z. Liu, Small 13 (2017) 1602456.

[262] B. Yu, W. Xing, W. Guo, S. Qiu, X. Wang, S. Lo, Y. Hu, J. Mater. Chem. A 4 (2016) 7330–7340.